Supplementary Materials for

All-printed soft human-machine interface for robotic physicochemical sensing

You Yu,[1]† Jiahong Li,[1]† Samuel A. Solomon,[1]† Jihong Min,[1] Jiaobing Tu,[1] Wei Guo,[1] Changhao Xu,[1] Yu Song,[1] Wei Gao[1]*

[1]Andrew and Peggy Cherng Department of Medical Engineering, Division of Engineering and Applied Science, California Institute of Technology, Pasadena, California, 91125, USA.

*Corresponding author. Email: weigao@caltech.edu.

†These authors contributed equally to this work.

Supplementary Methods

Diffusion dynamics of dry-phase analyte through the hydrogel

The simulation of the mass transport process for the dry-phase analyte through the hydrogel to the sensor's surface was conducted using finite element analysis (FEA) on the commercial software COMSOL Multiphysics. Tetrahedral elements with refined meshes allowed modeling of the source's diffusion in 3D space with testified accuracy. The fluid flow is described by the Navier-Stoke equation for incompressible flow

$$\rho\left(\frac{\partial v}{\partial t} + (v \cdot \nabla)v\right) = -\nabla p + \mu\nabla^2 v \quad (1)$$

$$\nabla \cdot v = 0 \quad (2)$$

And the convection diffusion is described by

$$\frac{\partial c}{\partial t} + v \cdot \nabla c = D\nabla^2 C \quad (3)$$

Where ρ, v, p and μ denote liquid density, flow velocity, pressure and viscosity respectively, whereas C and D denote the concentration and the diffusion coefficient. The diffusion coefficient of paraoxon, TNT, proton, sarin, and nitrogen mustard are 4.7×10^{-6} cm^2 s^{-1}, 6.7×10^{-6} cm^2 s^{-1}, 9.3×10^{-5} cm^2 s^{-1}, 8.6×10^{-6} cm^2 s^{-1} and 8.2×10^{-6} cm^2 s^{-1} respectively.

The source diffusion in the water tank was modeled using a chemical droplet hitting the water with an initial speed of 0.5 m s^{-1} perpendicular to the surface (with height of 0). A no-slip boundary condition was applied on all tank walls including the barriers.

For the dry phase detection simulation, hydrogels are modeled as liquids with no internal fluid flow. It is assumed that the target species (1 mM) completely dissolved into the hydrogels from the bottom and form a 20 μM concentrated solution layer at $t = 0$. The solute concentration detected by the electrode is tracked by computing the average concentration at the hydrogel's top surface (hydrogel-electrode interface). The simulated diffusion process is shown in **fig. S4**. The time request for complete diffusion will increase dramatically as the hydrogel's thickness increases. Thus, a thinner hydrogel layer will be appreciated for rapid dry phase detection. Moreover, among all simulated chemical species, protons diffuse much faster than all other species. It takes less than 30 s for protons to completely diffuse through the 0.5 mm hydrogel layer, which suggest the possibility of dry-phase pH monitoring.

Feature engineering and channel selection

The following five features were extracted from each peak (serialized gesture) found in the root mean squared (RMS) filtered EMG data: height, average area, standard deviation, average energy, and maximum slope. During feature extraction, each peak was referenced against its baseline, which was determined via a binary search of the previous data in 50 ms intervals. By skipping points, the algorithm ignored minor fluctuations in the peak's rise to find the local minimum

(baseline of the peak). To decrease the delay time in gesture recognition, only points between the baseline and the top of the peak were analyzed. The five features extracted are defined as follows:

$$Peak\ Height: RMS[peakIndex] - RMS[leftBaselineIndex] \quad (4)$$

$$Peak\ Average: \frac{\sum_{i=leftBaselineIndex}^{i=peakIndex}[RMS_i]}{N} \quad (5)$$

$$Peak\ Standard\ Deviation: \frac{\sqrt{\sum_{i=leftBaselineIndex}^{i=peakIndex}[RMS_i - \mu_{RMS}]^2}}{N-1} \quad (6)$$

$$Average\ Peak\ Energy: \frac{\sum_{i=leftBaselineIndex}^{i=peakIndex}[RMS_i]^2}{N} \quad (7)$$

$$Maximum\ Peak\ Slope: \max(gradient(RMS[peakIndex: leftBaselineIndex + 1])) \quad (8)$$

Where peakIndex and leftBaselineIndex represent the indices of the peak's maximum and left baseline in the RMS data respectively; μ_{RMS} is the peak average; and N is the number of RMS points between the peak and its baseline.

After data collection and feature extraction, the performance enhancement of each feature and channel for accurate gesture classification was evaluated using Shapley additive explanation (SHAP) values, which utilizes a game theory approach to explain a feature's individual and overall contribution to the final prediction. Effectively, the SHAP value of a feature represents the average marginal contribution of the feature across the entire dataset (all prediction instances). In addition to SHAP values, the average testing accuracy across 5000 trials was taken for each permutation of features and channels, which supplemented the SHAP values in providing further insight into which channels and features contained non-overlapping beneficial information for gesture determination. For each of the 5000 runs, the testing points represented 33% of the dataset, with each gesture in the test set being proportionally represented in the full dataset.

Notable feature permutations, with and without 1 channel removed, from the arm EMG dataset is displayed in **table S2.** As shown in the table, out of each feature, peak height and standard deviation classified the 6 gestures the best with the highest mean accuracy and lowest standard deviation (when evaluated by themselves). On the contrary, peak energy, which holds a good amount of gesture information with an 88.71% classification accuracy, is the least import feature, with the lowest mean accuracy and greatest standard deviation. The relatively high accuracy for each feature substantiates the assumption that each peak property contains useful information about motor intention, validating their use in the KNN model. Based solely on the table values, however, there appears to be no statistically significant feature pairing that improves the classification accuracy above using peak height or standard deviation alone. The table additionally shows that channel 1 appears to be the least important channel, while channels 2 and 3 seems to be the most important channels for accurate motor classification.

This information is expanded upon when looking at the SHAP analysis. Despite no statistically significant accuracy change in **table S2**, using both STD and PH together can alleviate the model's

reliance on only one parameter. When only considering PH in **fig. S31A**, each channel's feature can drastically alter the final gesture prediction. Such volatility can be contrasted when the STD feature is added in **fig. S31D**. With PH and STD, the decision tree spreads out more at the base, reducing the model's reliance on any one feature. The perceived advantage of adding another feature is further exemplified when analyzing each feature pairing with PH (**fig. S31B–E**). When pairing PE or MS with PH, the model does not effectively utilize the added feature (negligible SHAP values). However, STD and PA are both relevant even when paired with PH, as seen by the tree spreading early. Even though the final classification remains the same, when pairing PH with STD or PH with PA, the model is more certain on the endpoint with each step and thus reduces the effect of a bad feature. For this reason, we recommend using PH, STD, and PA together (**fig. S31F**), to add as much novel information to the model while reducing the reliance on any one parameter.

In addition to proper feature extraction, another component to consider in gesture classification is the number of channels collecting data. While one can obtain a higher accuracy from using more data channels, it is advantageous to reduce the amount of hardware present on the patient's body for comfort and affordability. The number of channels needed to maintain a high classification accuracy was evaluated in **table S3**. As shown in the table, with the highest classification accuracy of 87.37%, there is a 10% accuracy decrease when only 2 channels are considered. For two channels, the most important combinations are channels 3 and 4, 2 and 4, as well as 2 and 3. Channel 1 is the least significant channel (as previously seen in **table S2**). The reason that channel 1 may not hold much information is because it is activated in almost every gesture. Because of this, it provides the most overlapping points across all the hand movements (the hardest to segment into classification groups). Meanwhile channels 3 and 4 (which represent the highest mean and lowest standard deviation), contains the least amount of activation for any gesture. Therefore, these channels carry a lot of weight when activated.

Combining the analysis from **tables S2 and S3**, the optimal number of channels to use is three channels, with two channels reducing the accuracy by at least 10%. For the highest accuracy, adding a fourth channel does have a marginal benefit to the mean (though not statistically significant). The authors decided to use four channels as the purpose of the experiment was to maximize the accuracy for remote robotic control. However, it can be appreciated that the same experiment could have been performed on 3 channels.

M-Boat searching algorithms

In choosing an efficient and intelligent search algorithm, 6 different algorithms were developed and compared against each other. The simplest model between them is the random direction (RD) algorithm, which acts as a baseline for searching the space with no intelligence. In this algorithm, the M-Boat chooses an arbitrary direction to move in at each point. If the potential movement would cause the M-Boat to go outside the tank, the angle is ignored, and another direction is randomly chosen. The algorithm with the next level of intelligence is the maximum direction (MD) model. At each step in this algorithm, the MD boat turns towards the sensor with the maximum

recorded value. The M-Boat will therefore only move in three distinct directions, representing the three sensor angles on the M-Boat, as shown in **fig. S42.** Each direction is calculated from the center of the boat to the edge of the highest-value sensor. However, if all the sensors record the same value, the algorithm will want to stay in its current location. For this edge case, the algorithm will inform the M-Boat to continue moving in its current direction (go straight). This model is very similar to the next method – the weighted maximum direction (WMD) algorithm. However, instead of using the maximum sensor's direction, each direction is weighted based on the sensor's value. To understand the mathematical discrepancies, the formulas for the maximum direction and weighted maximum direction algorithms is provided below:

$$MD = max(S_1, S_2, S_3)\,[0{:}\,2] \tag{9}$$

$$WMD = \sum_{i=1}^{3} S_i[0{:}\,2] * S_i[2] \tag{10}$$

Where S_i is the i^{th} sensor on the M-Boat, which is represented as a tuple of coordinates. The first two indices in the tuple are the X and Y locations of the M-Boat in the tank respectively and the last index is the sensor's reading ($S = \langle X_{Loc}, Y_{Loc}, Sensor\ Value \rangle$).

Instead of relying solely on the three chemical sensors to make a movement decision, the final three models use more intelligent algorithms that attempt to reconstruct part of the concentration profile in the tank. The interpolated map (IM) algorithm achieves this by using the last three readings to estimate the immediate concentration gradient around the M-Boat. The decision to only use three previous results instead of every recording stems from factors altering the concentration profile such as natural diffusion and induced diffusion as the M-Boat propels itself forwards. In the model, the space is mapped using linear interpolation with the griddata function from SciPy (version 1.4.1). After estimating the concentration profile, the M-Boat will move to the direction with the highest interpolated concentration. If all the values are the same, then the M-Boat will continue moving straight.

The gradient descent method similarly tries to reconstruct the concentration curve but achieves this through calculating the gradient at the current boat's position. In calculus, the gradient is defined as the direction of maximum increase in the 2D contour plane. On a 3D curve, where the XY plane represents the water's surface and the Z-direction represents the chemical's concentration, the direction of maximum increase would be the direction the M-Boat should travel to find the chemical's source. We will define the concentration at any given XY location as C(x,y) and the M-Boat's current location as x_0, y_0. With this information, the 2D gradient in the contour plane can be defined as follows:

$$Gradient = \overrightarrow{\nabla C}(x_0, y_0) = \left[\left.\frac{dC(x,y_0)}{dx}\right|_{x=x_0}, \left.\frac{dC(x_0,y)}{dy}\right|_{y=y_0} \right] \tag{11}$$

While the full concentration curve, C(x,y), is not known during the search, at each step, the sensor will record three points in C(x,y) around x_0, y_0 (the M-Boat's current location). One can therefore still extrapolate key information about the concentration curve at the M-Boat's location using these points.

With the sensor values, one can calculate the tangent plane at $C(x_0, y_0)$. To evaluate the concentration around the M-Boat, we first create a 3D function to calculate the gradient: F(x,y,z) = C(x,y) – z. With this new form, the general equation of the tangent plane can be defined as follows:

$$\left.\frac{dF(x,y_0,z_0)}{dx}\right|_{x=x_0}(x-x_0)+\left.\frac{dF(x_0,y,z_0)}{dy}\right|_{y=y_0}(y-y_0)+\left.\frac{dF(x_0,y_0,z)}{dz}\right|_{z=z_0}(z-z_0)=0 \quad (12)$$

Rearranging the equation above, we get:

$$\left\langle\left.\frac{dF(x,y_0,z_0)}{dx}\right|_{x=x_0},\left.\frac{dF(x_0,y,z_0)}{dy}\right|_{y=y_0},\left.\frac{dF(x_0,y_0,z)}{dz}\right|_{z=z_0}\right\rangle\cdot\langle x-x_0,y-y_0,z-z_0\rangle=0 \quad (13)$$

As X, Y, Z and x_0, y_0, z_0 are both in the plane, the second term defines any arbitrary vector that is confined to the plane. Therefore, the first term $\left\langle\left.\frac{dF(x,y_0,z_0)}{dx}\right|_{x=x_0},\left.\frac{dF(x_0,y,z_0)}{dy}\right|_{y=y_0},\left.\frac{dF(x_0,y_0,z)}{dz}\right|_{z=z_0}\right\rangle$ represents the set of all vectors that are perpendicular to the plane, commonly referred to as the normal direction of the plane. This perpendicular direction can be calculated through the cross product of any two coplanar vectors. By defining the location of one sensor as $\langle S_{1x}, S_{1y}, S_{1z}\rangle$, two coplanar vectors in the tangent plane can be calculated as follows:

$$\vec{A}=\langle \mathrm{S_{1x}}-S_{2x}, S_{1y}-S_{2y}, S_{1z}-S_{2z}\rangle \; and \; \vec{\mathrm{B}}=\langle \mathrm{S_{1x}}-S_{3x}, S_{1y}-S_{3y}, S_{1z}-S_{3z}\rangle \quad (14)$$

Where the cross product (the normal vector) is calculated as:

$$\vec{A}\times\vec{\mathrm{B}}=\begin{vmatrix}\hat{\imath} & \hat{\jmath} & \hat{k}\\ \mathrm{S_{1x}}-S_{2x} & S_{1y}-S_{2y} & S_{1z}-S_{2z}\\ \mathrm{S_{1x}}-S_{3x} & S_{1y}-S_{3y} & S_{1z}-S_{3z}\end{vmatrix}=Normal\ Vector \quad (15)$$

Substituting F(x,y,z) = C(x,y) – z back, one gets:

$$\begin{aligned}Normal\ Vector &= \left\langle\left.\frac{dF(x,y_0,z_0)}{dx}\right|_{x=x_0},\left.\frac{dF(x_0,y,z_0)}{dy}\right|_{y=y_0},\left.\frac{dF(x_0,y_0,z)}{dz}\right|_{z=z_0}\right\rangle\\ &= \left\langle\left.\frac{dC(x,y_0)}{dx}\right|_{x=x_0},\left.\frac{dC(x_0,y)}{dy}\right|_{y=y_0},-1\right\rangle \quad (16)\end{aligned}$$

The projection of the normal vector onto the X-Y plane is shown to be the gradient, representing the direction with the highest local concentration. For the gradient descent method, the above algorithm is performed at every decision point. If the gradient is too small to consider, the M-Boat does not change directions (it moves straight).

While the gradient descent method approximates the direction of maximum increase, this algorithm does not take advantage of past information. Meanwhile, the IM algorithm utilizes past information to interpolate what to do in the future. The A* approach utilized both algorithms together with equal weight to make a well-informed decision on where the M-Boat should move next using past and present information.

These various source-locating algorithms were simulated on the M-Boat to find the location of any chemical spill optimally and reliably. The M-Boat was further evaluated in the case of multiple

leaks. As shown in **fig. S41D** and **E**, for two leakage sources, the maximum direction and gradient descent algorithms will preferentially find the closest source to its current location. This is because these algorithms only rely on data calculated from its current position, moving in the direction of maximum increase (which is biased by the closest chemical spill). In contrast, the interpolated map, which is used as a heuristic in the A* algorithm, takes advantage of previous points to map the space around the boat. Hence, after multiple steps, the algorithm realizes (interpolates) that there are two sources ahead. Through the interpolation, the algorithm can further differentiate which one is larger. As shown in **fig. S41D**, initially, the four algorithms follow the same path. However, after a few steps, the interpolated map and A* algorithms diverge towards the maximum source. For each algorithm, the path to the source is not direct as the data at any location is a superposition of both sources, which causes a distortion in the map where the sources overlap (seen as the saddle point). The degree to which the A* algorithm will diverge to either source was further evaluated in **fig. S41E**, where various start points were selected.

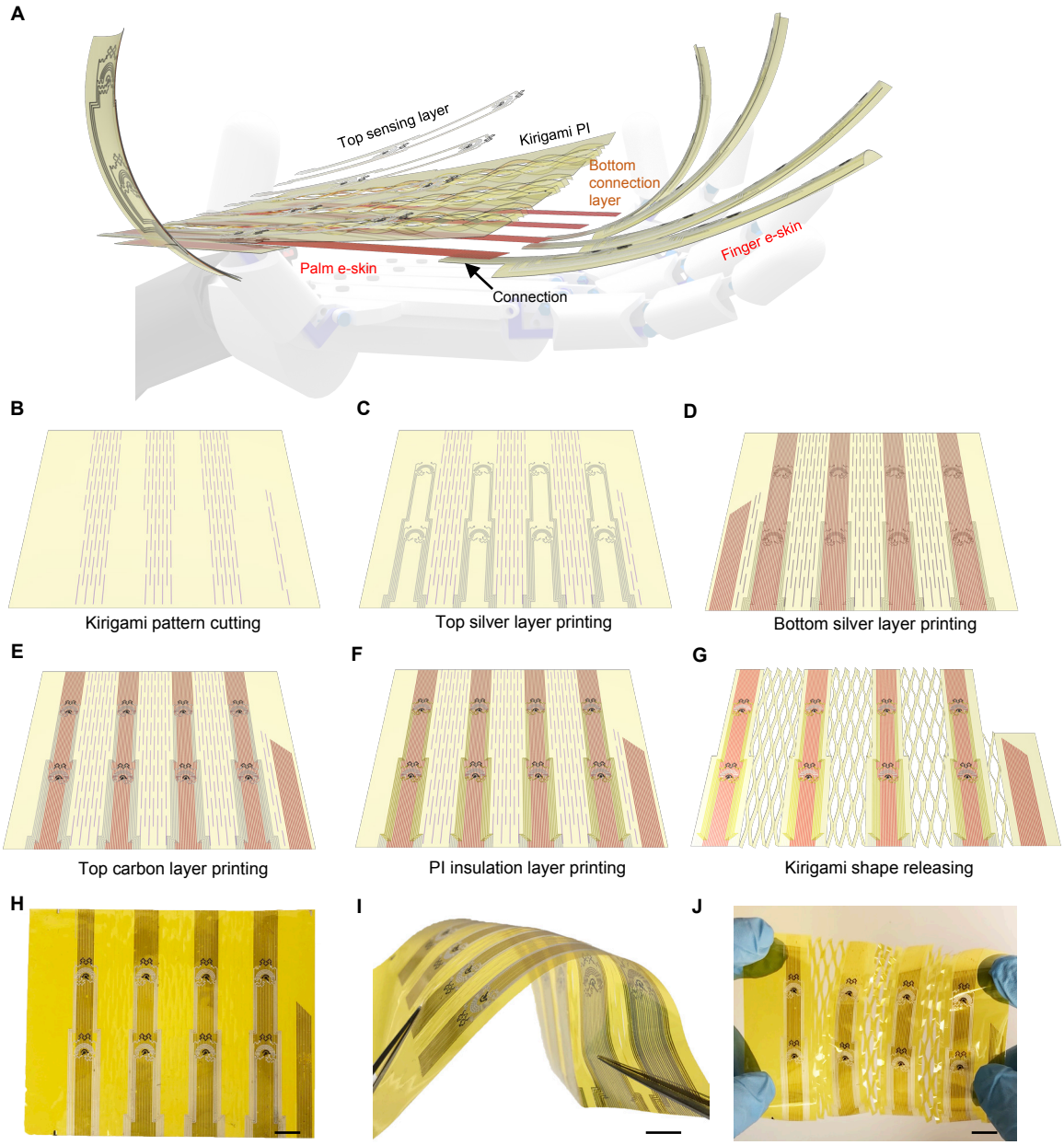

Fig. S1. Schematic and fabrication procedure of e-skin-R. (**A**) Schematic of a robotic hand-interfaced soft kirigami e-skin-R patch. (**B–G**), Fabrication process of the soft e-skin with automatic kirigami cutting and inkjet printing. (**H–J**) Photographs of an e-skin-R under flat (**H**), bended (**I**), and stretched (**J**) conditions. Scale bars, 1 cm.

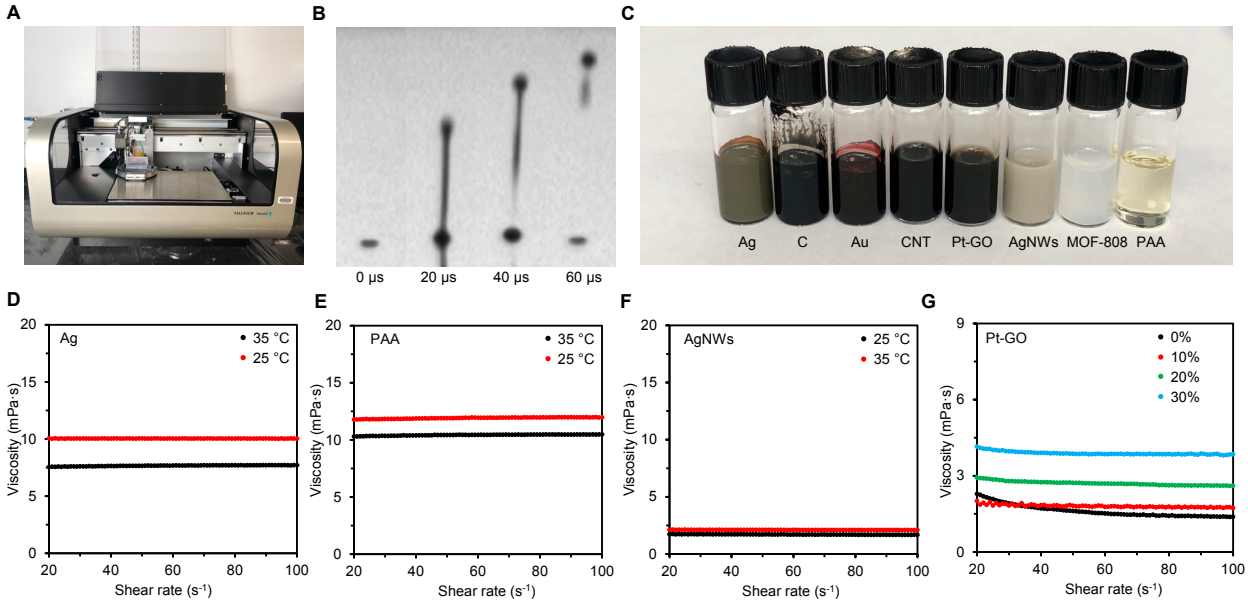

Fig. S2. Characterization of drop-on-demand inkjet printing with custom-designed inks. (**A**) Photograph of the inkjet printer (Dimatix Materials Printer DMP-2850). (**B**) Time lapse images of a 10-pl ink droplet ejected from the printer head. Ink, PAA. (**C**) Photograph of the nanoengineered inks used to prepare the M-Bot. (**D–F**) The viscosities of Ag (**D**), PAA (**E**), and AgNWs (**F**) inks under 25 °C and 35 °C. (**G**) The viscosities of Pt-GO inks with propylene glycol ranging from 0% to 30% (v:v).

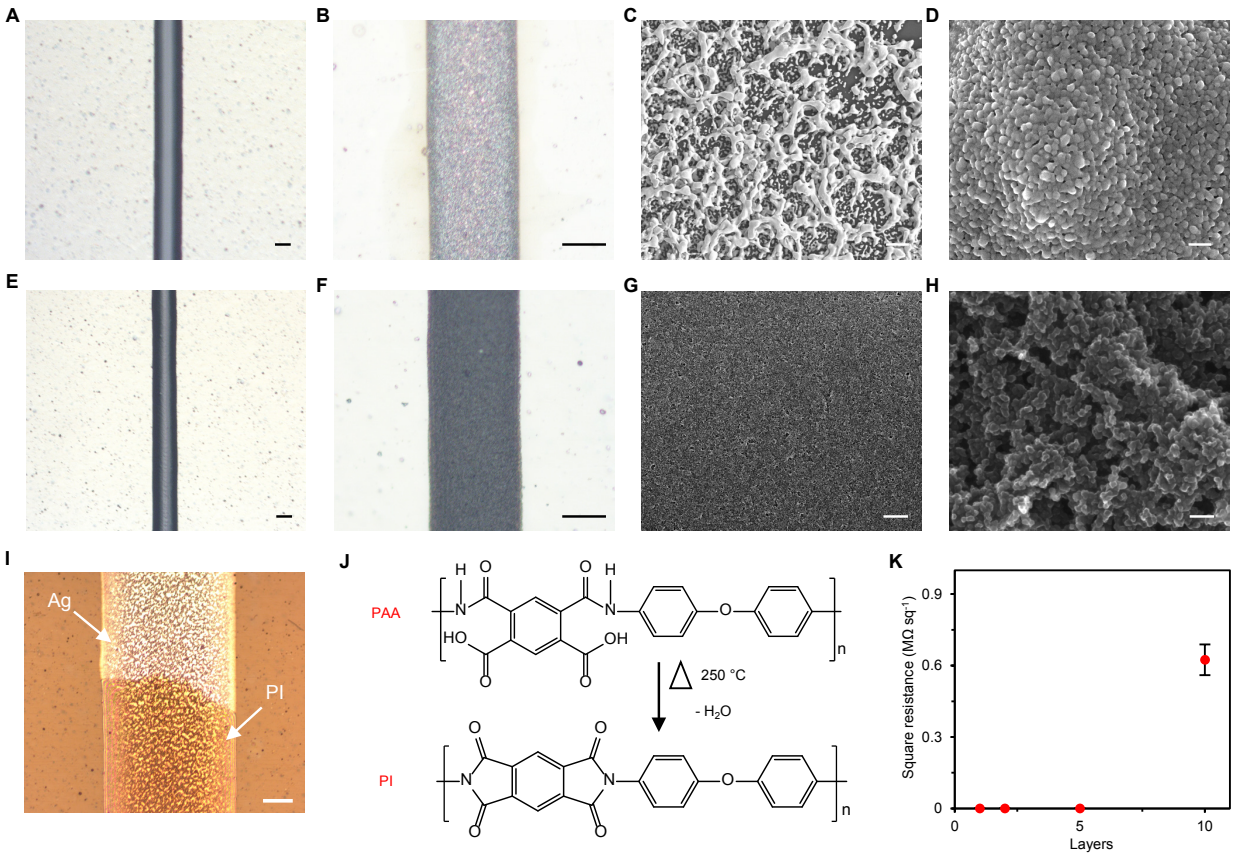

Fig. S3. Characterizations of inkjet-printed nanostructured patterns for M-Bot. (A and **B)** Microscopic images of a printed silver interconnect before (**A**) and after (**B**) annealing. Scale bars, 10 µm. (**C** and **D**) SEM images of a printed silver interconnect after annealing. Scale bars, 10 µm and 100 nm, respectively. (**E** and **F**) Microscopic images of a printed carbon pattern before (**E**) and after (**F**) annealing. Scale bars, 10 µm. (**G** and **H**) SEM images of a printed carbon pattern after annealing. Scale bars, 5 µm and 100 nm, respectively. (**I**) Microscopic image of a partially PI insulated silver interconnect after annealing. Scale bar, 40 µm. (**J**) Thermal transformation of PAA ink to PI insulation layer during thermal annealing. (**K**) Square resistance of the PI insulation films printed with different layers. Error bars represent the s.d. from 3 measurements.

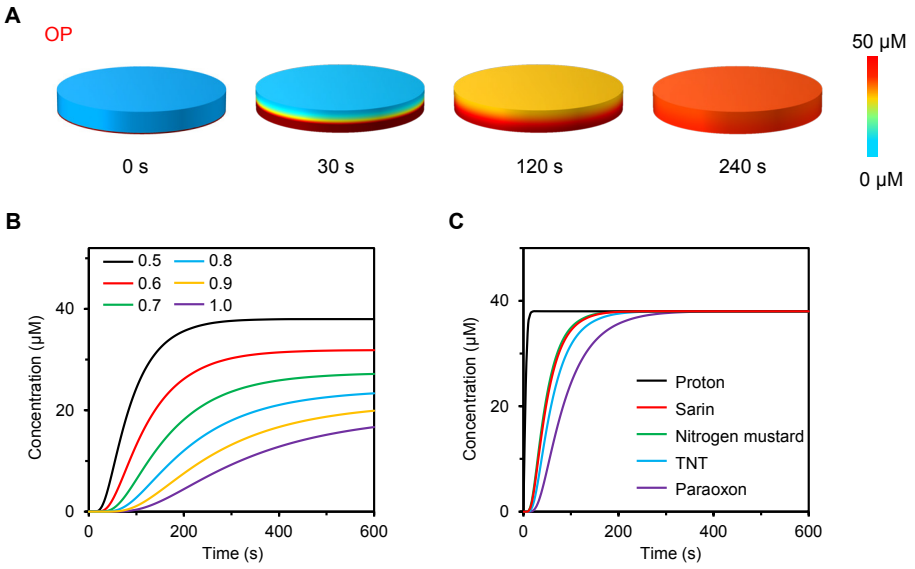

Fig. S4. Simulation of the hydrogel-based solid-phase hazard analyte sampling and sensing. (**A**) Simulated diffusion dynamics of a hazard chemical (OP) though a 0.5-mm thick hydrogel. (**B**) Simulated time-dependent of OP concentrations at the electrode's surface coated with hydrogels of various thickness (0.5–1 mm). (**C** and **D**) Simulated time-dependent levels of hazard chemicals (proton, sarin, nitrogen mustard, TNT, paraoxon) at the sensor's surface coated with a 0.5-mm thick hydrogel.

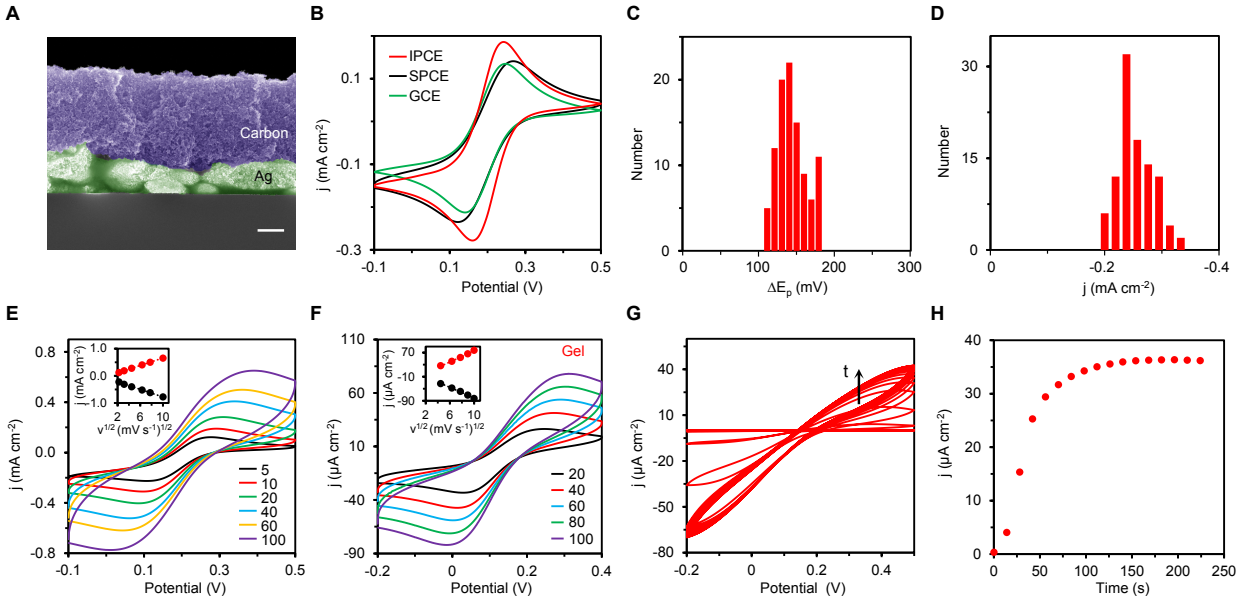

Fig. S5. Characterizations of the IPCEs. (**A**) Cross-sectional scanning electron microscopy (SEM) image of an IPCE. Scale bar, 1 μm. (**B**) CVs of an IPCE, a screen print carbon electrode (SPCE), and a glassy carbon electrode (GCE) in 5 mM $K_3Fe(CN)_6$. Scan rate, 5 mV s^{-1}. (**C** and **D**) Distributions of redox peak potential differences (ΔE_p) (**C**) and reduction peak current densities (j) (**D**) in the cyclic voltammograms (CVs) of 100 IPCEs in 5 mM $K_3Fe(CN)_6$. Scan rates, 5 mV s^{-1}. (**E** and **F**) CVs of an IPCE in 5 mM $K_3Fe(CN)_6$ (**E**) and an IPCE coated with a hydrogel containing 2 mM $K_3Fe(CN)_6$ (**F**) under different scan rates. Insets, the corresponding current peak densities plotted against the square root of the scan rates ($v^{1/2}$). Scan rates, 5–100 mV s^{-1}. (**G** and **H**) The CVs (**G**) and the time-dependent oxidation peak current densities (**H**) obtained after adding 8 μg $K_3Fe(CN)_6$ onto a hydrogel-loaded IPCE (final equilibrium concentration is ~2 mM). Scan rates, 100 mV s^{-1}.

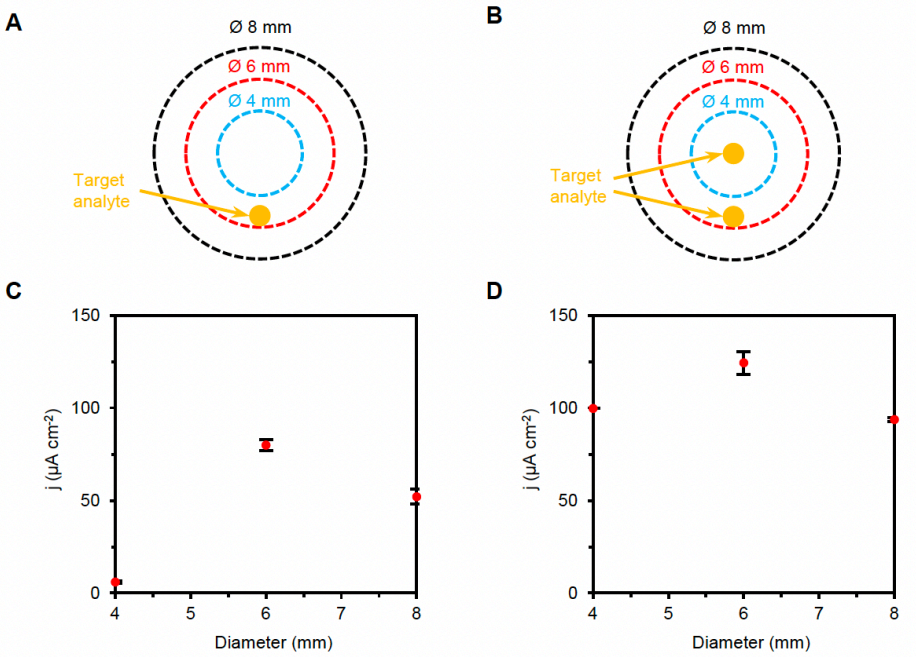

Fig. S6. **Evaluation of the M-Bot chemical sensing using hydrogels with enlarged size.** (**A–D**) Illustrations of dry-phase target analyte detection using hydrogels with different sizes (**A** and **B**) and the corresponding current responses of the IPCEs (**C** and **D**). j, oxidation peak current density of the CVs of the IPCEs (scan rate, 50 mV s^{-1}). Dry-phase $K_3Fe(CN)_6$ (8 μg) was used as the target analyte. Error bars represent the s.d. from 3 sensors.

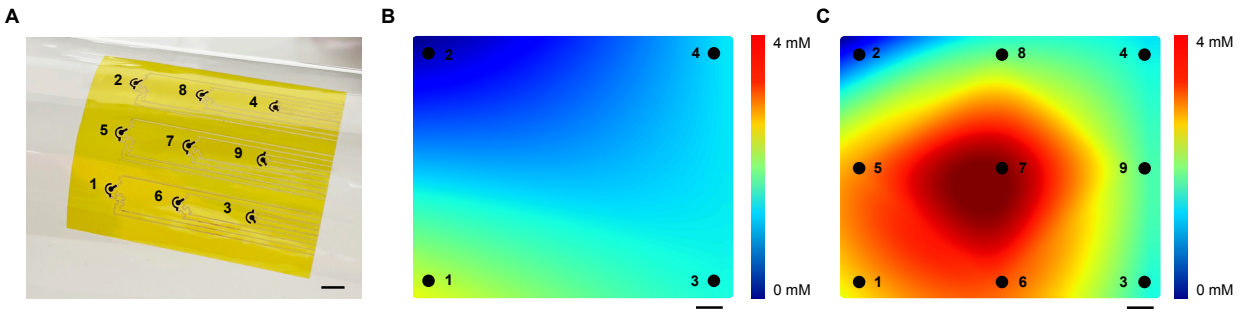

Fig. S7. **Evaluation of the M-Bot chemical sensing with increased sensor density.** (**A**) Photograph of an IPCE sensor array with 9 chemical sensors. Scale bar, 5 mm. (**B** and **C**) The color mappings of target distributions generated by 4 sensors (**B**) and 9 sensors (**C**). Scale bars, 2 mm. The target analyte – $K_3Fe(CN)_6$ – was spray-coated around the center of the detection area.

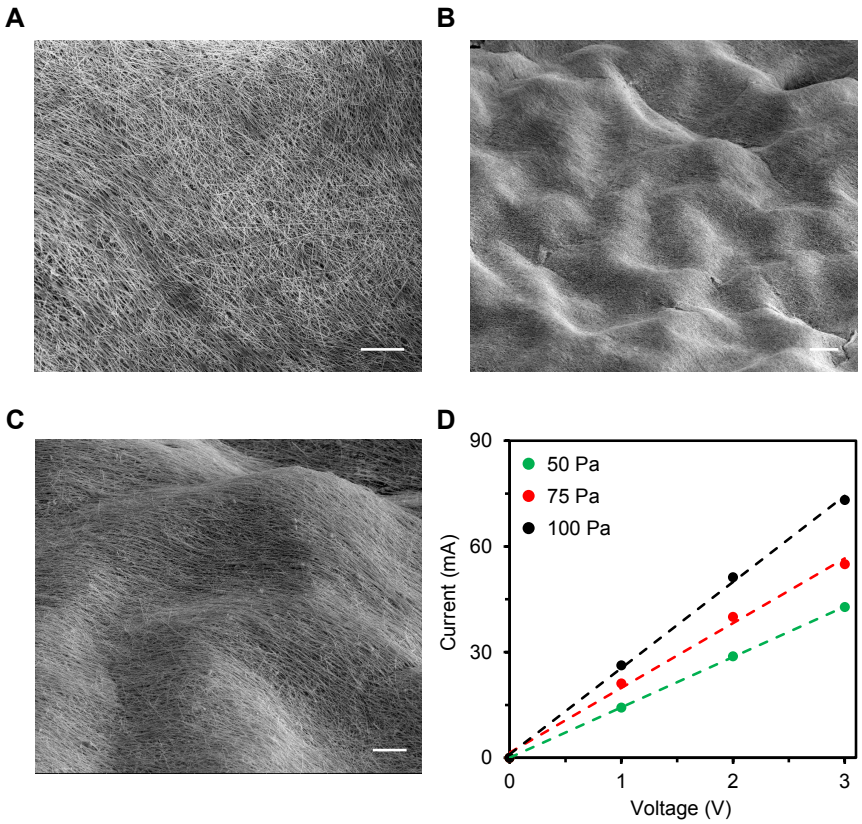

Fig. S8. Characterization of the printed AgNWs/N-PDMS tactile sensors. (**A–C**) SEM images of inkjet-printed AgNWs on a nanotextured PDMS substrate. Images were taken with a substrate angle of 52°. Scale bars, 10, 20, and 10 μm, respectively. (**D**) Current response of a tactile sensor under varied pressure and voltage loads.

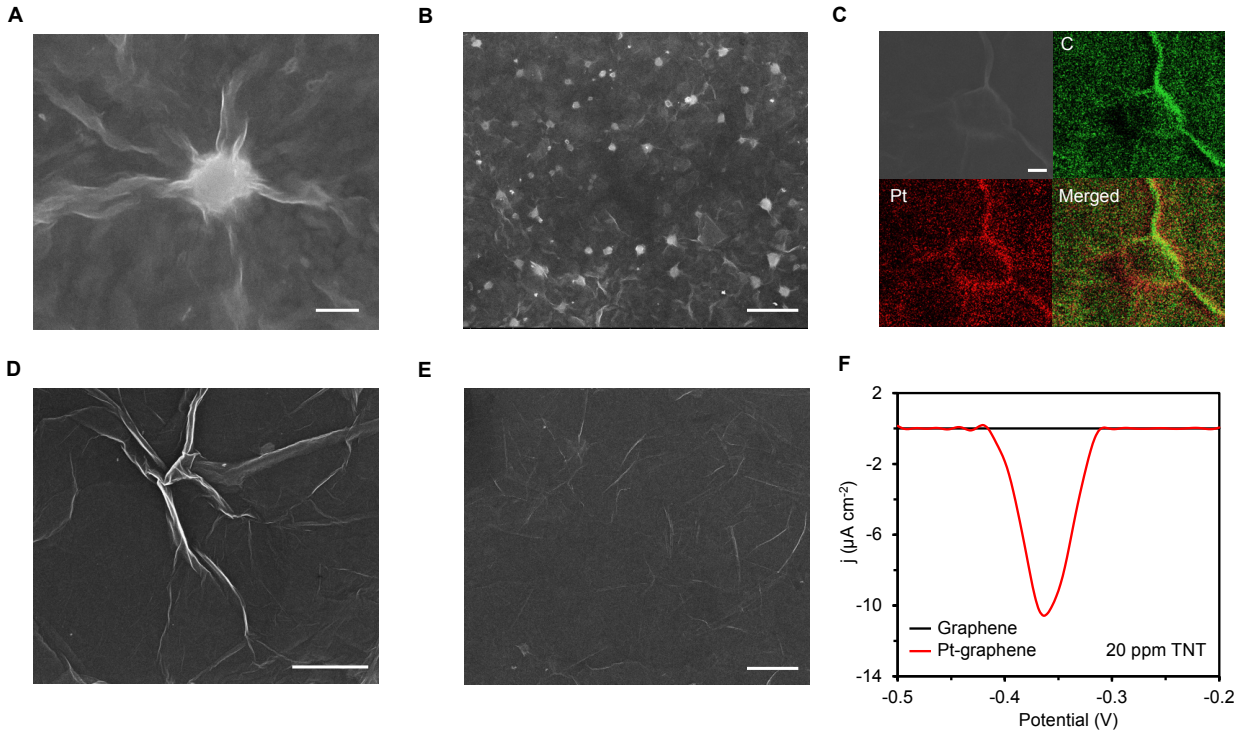

Fig. S9. Characterization of printed Pt-graphene electrodes. (**A** and **B**) SEM images of an inkjet-printed Pt-graphene electrode. Scale bars, 1 and 5 µm, respectively. (**C**) Energy dispersive X-Ray analysis (EDX) of a printed Pt-graphene electrode. Scale bar, 1 µm. (**D** and **E**) SEM images of inkjet-printed graphene electrode. Scale bars, 1 and 3 µm, respectively. (**F**) nDPV voltammograms of a printed Pt-graphene electrode and a graphene electrode in 20 ppm TNT.

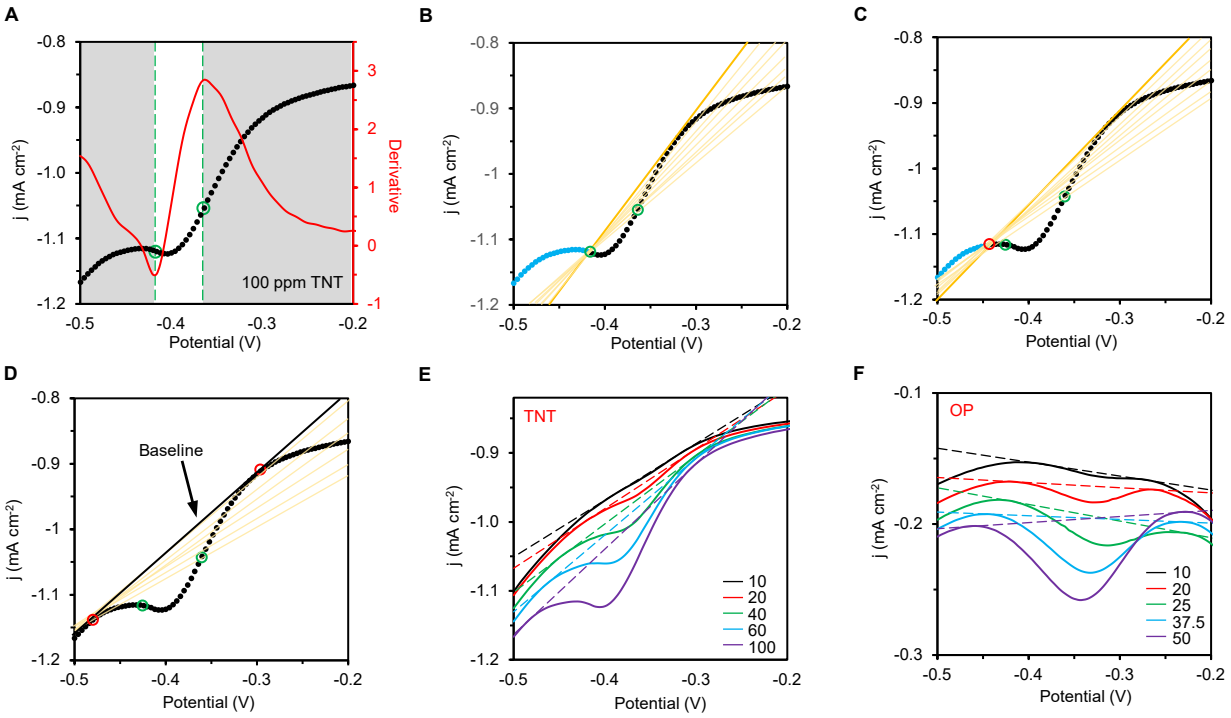

Fig. S10. The algorithm used for automatic baseline correction of the DPV voltammograms. (**A**) DPV voltammograms of TNT detection (black) and its corresponding first derivative (red). The DPV curve can be divided into three segments by the inflection points (green), where the DPV peak will fall into the middle-highlighted region. (**B**) Beginning with the left inflection point, multiple lines (yellow) were extended to points in the right region through linear fitting to find the tangent line to the curve on the right hand side. The data points to the left (blue) were above all lines defined in this case. (**C**) Using the tangent point, and repeating the steps described in part **B**, the red point next to the left inflection point was chosen as the new center point. The procedure in part b was repeated with this new center point. If there exist data points that are above all lines defined in this case, the next point will be chosen as the center point and the same procedure will be applied again. (**D**) Eventually, one line above all data points (defined by the two data points shown in red) will be found, and this line will be taken as the baseline (thick black line) to the DPV curve. (**E**) DPV voltammograms of TNT detection and their baselines defined by this algorithm. (**F**) DPV voltammograms of OP detection and their baselines defined by this algorithm.

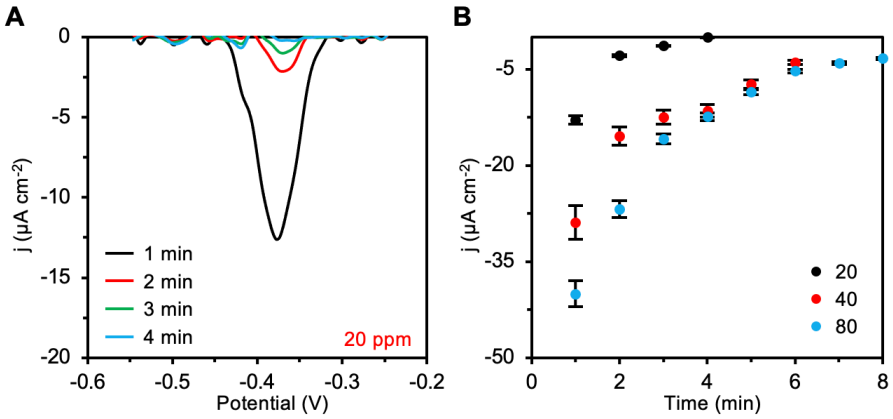

Fig. S11. In situ regeneration of the hydrogel-loaded Pt-graphene TNT sensors. (**A**) nDPV voltammograms of the regeneration process for a Pt-graphene sensor coated with a hydrogel containing 20 ppm TNT. (**B**) Peak current densities of the nDPV voltammograms of the regeneration process for Pt-graphene sensors coated with hydrogels containing 20, 40, and 80 ppm TNT. Error bars represent the s.d. from 3 sensors.

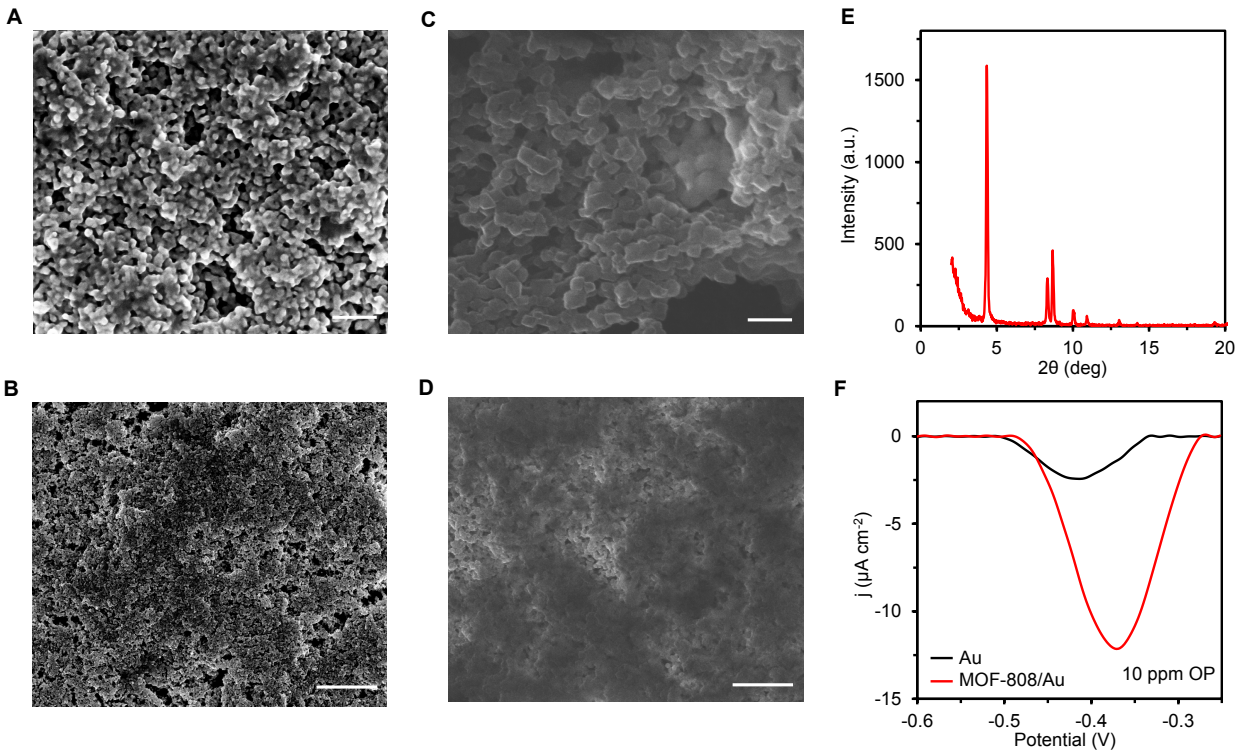

Fig. S12. Characterization of the printed MOF-808/Au electrodes. (**A** and **B**) SEM image of inkjet-printed Au nanoparticles. Scale bars, 200 nm, and 2 μm. (**C** and **D**) SEM image of inkjet-printed MOF-808/Au. Scale bars, 100 nm, and 500 nm. (**E**) XRD curve of MOF-808. (**F**) DPV voltammograms of printed MOF-808-Au and Au electrodes in 10 ppm OP.

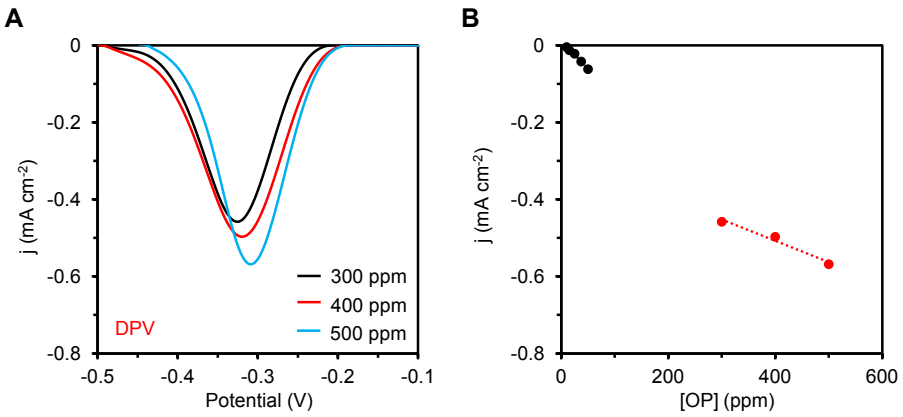

Fig. S13. **Evaluation of the MOF-808/Au electrode for high-concentration OP analysis.** (**A** and **B**) nDPV voltammograms of a MOF-808/Au OP sensor in the presence of high-concentration OP (300–500 ppm) (**A**) and the corresponding calibration curve (**B**). Black points in **B** represent the data collected in low-concentration range.

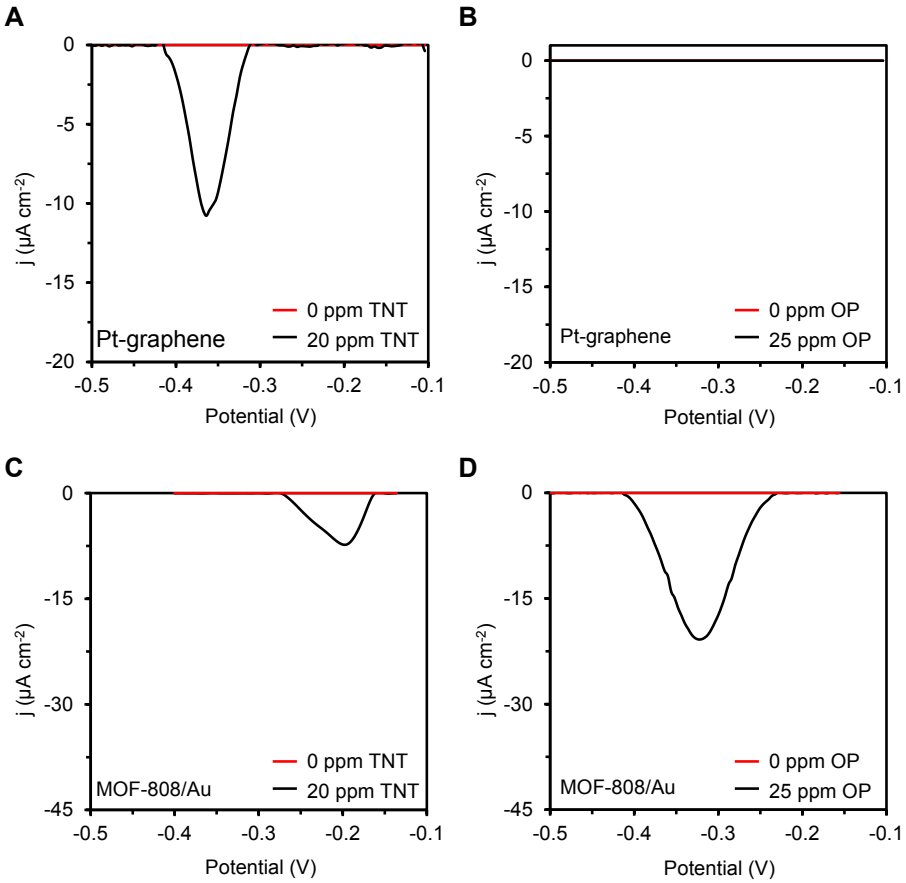

Fig. S14. **The selectivity of Pt-graphene and MOF-808/Au electrodes over OP and TNT. (A–D)** nDPV voltammograms of a Pt-graphene sensor (**A** and **B**) and a MOF-808/Au sensor (**C** and **D**) in 20 ppm TNT and 25 ppm OP.

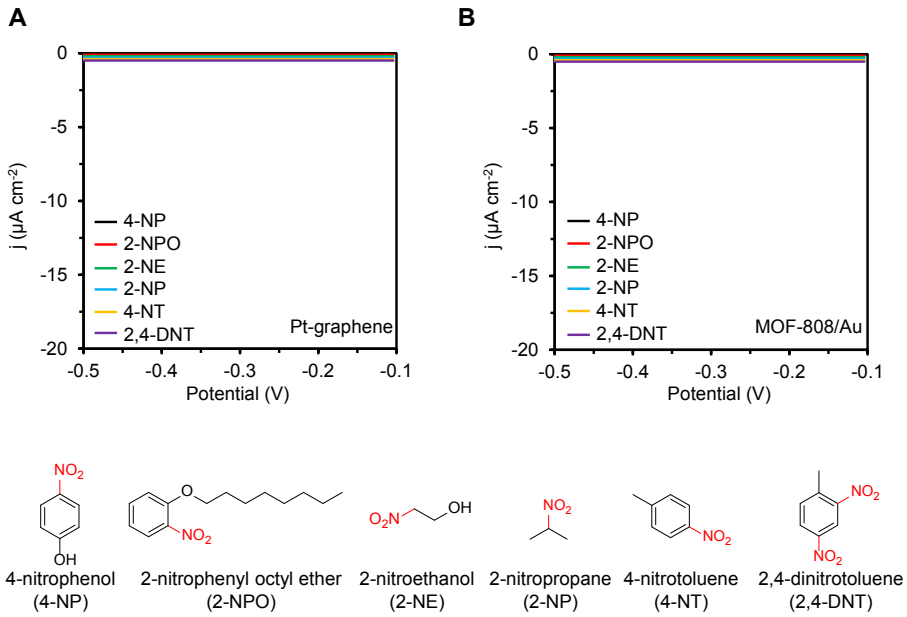

Fig. S15. **The selectivity of TNT and OP sensors over other nitro compounds. (A** and **B)** nDPV voltammograms of a Pt-graphene TNT sensor (**A**) and a MOF-808/Au OP sensor (**B**) in 20 ppm six different types of nitro compounds.

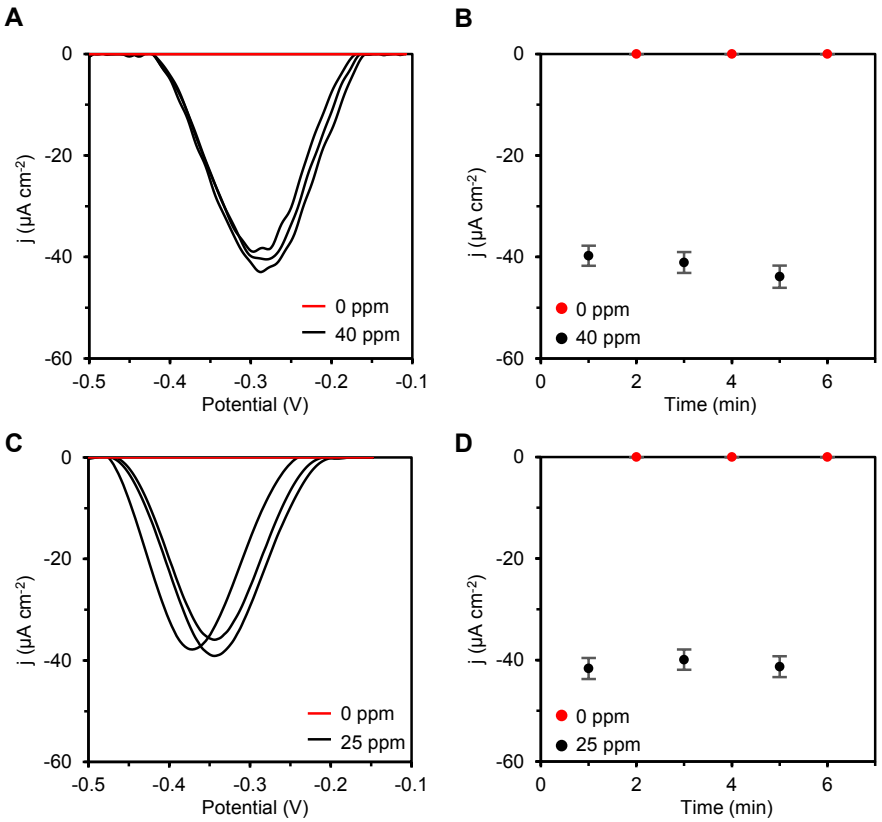

Fig. S16. **The continuous TNT and OP sensing with the printed TNT and OP sensors.** (**A** and **B**) nDPV voltammograms of the Pt-graphene TNT sensors (**A**) and corresponding peak current heights (**B**) obtained continuously 0 and 40 ppm TNT. (**C** and **D**) nDPV voltammograms of the MOF-808/Au OP sensors (**A**) and corresponding peak current heights (**B**) obtained continuously in 0 and 25 ppm OP. Error bars represent the s.d. from 3 sensors.

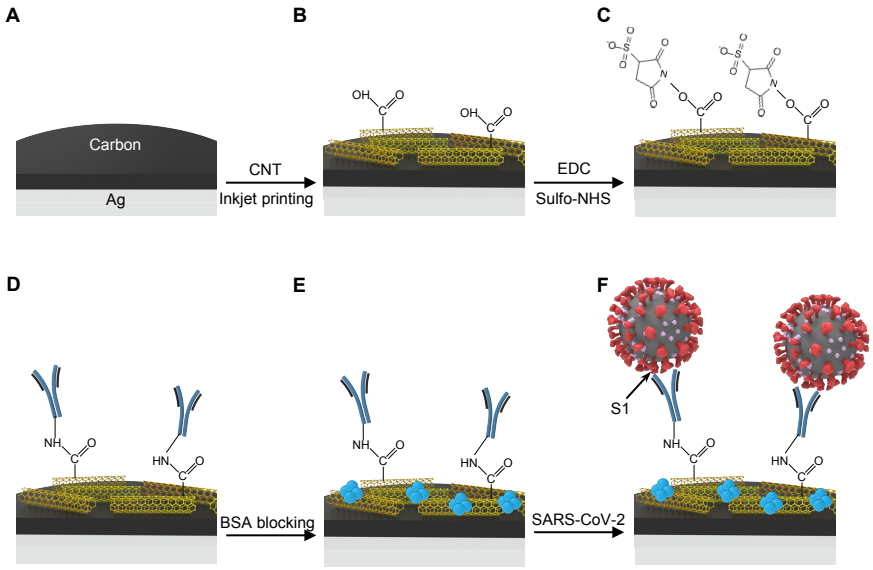

Fig. S17. Schematic of the modification procedure of the printed CNT electrode for SARS-CoV-2 S1 sensing.

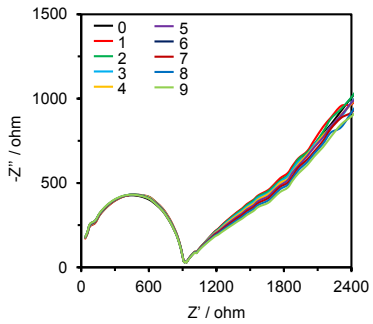

Fig. S18. **Evaluation of the stability of antibody immobilization.** Nyquist plots of a CNT-based SARS-CoV-2 S1 sensor in 5 mM $K_3Fe(CN)_6$ before and after repetitive washing steps. Electrochemical impedance spectroscopy tests were performed at open circuit potentials with an AC amplitude 5 mV in the range of 0.1–10^6 Hz.

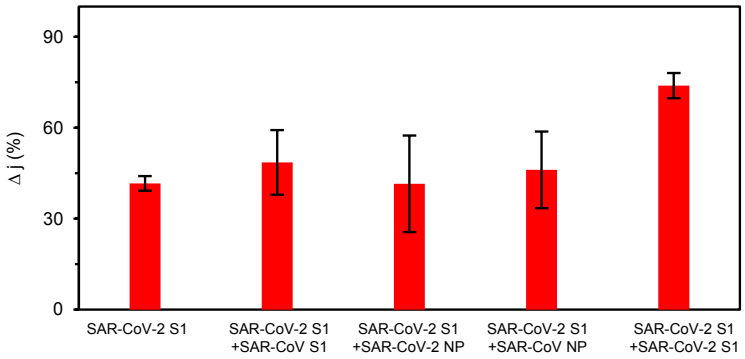

Fig. S19. **The selectivity of the SARS-CoV-2 S1 sensor over other viral proteins.** Δj, percentage DPV peak current changes after target incubation. Error bars represent the s.d. from 3 sensors. 500 ppb interference proteins were added into 500 ppb SARS-CoV-2 S1. NP, nucleocapsid protein.

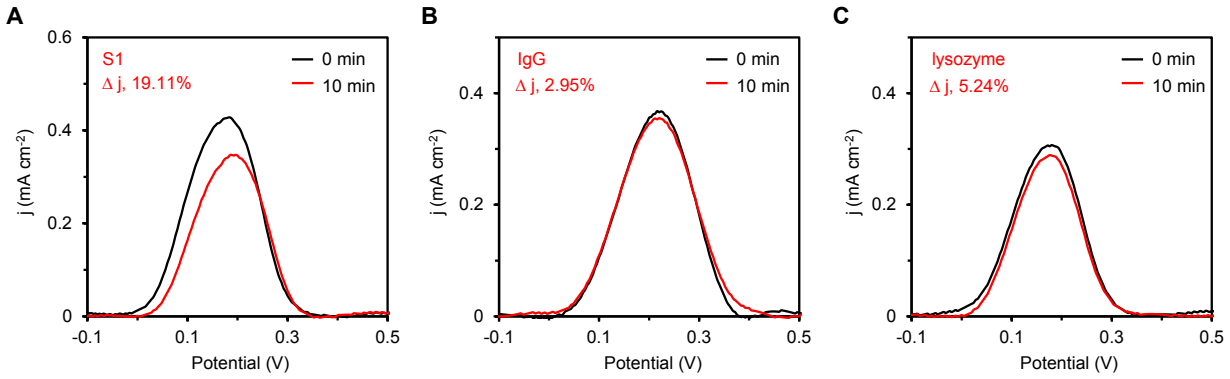

Fig. S20. **The selectivity of the SARS-CoV-2 S1 sensor for dry-phase protein detection.** (**A**–**C**) DPV voltammograms of the SARS-CoV-2 S1 sensors before and after incubation with 10 ng dry-phase SARS-CoV-2 S1 (**A**), human immunoglobulin G (IgG) (**B**), and lysozyme (**C**). Inset values show percentage DPV peak current changes before and after incubation.

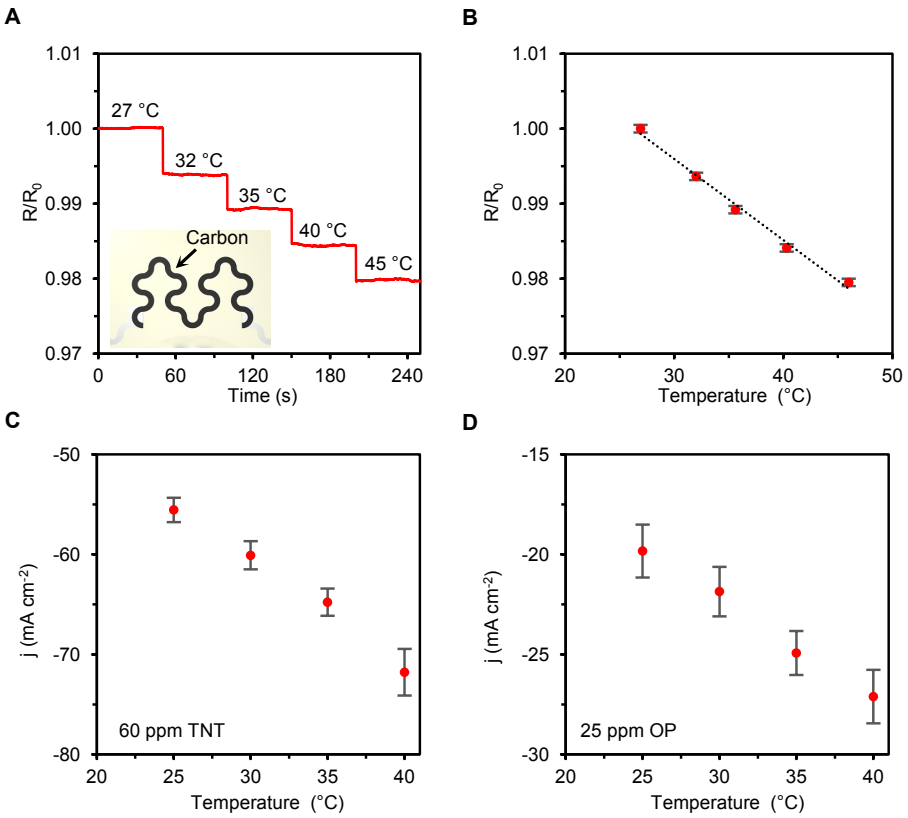

Fig. S21. Characterization of printed carbon-based temperature sensor toward real-time temperature sensing and calibration. (**A** and **B**) Dynamic response (**A**) and calibration plot (**B**) of the inkjet-printed carbon based temperature sensor. Inset, schematic of the carbon temperature sensor. R and R_0 represent the resistive response of the sensors after and before bending, respectively. (**C** and **D**) The performance of a TNT sensor (**C**) and an OP sensor (**D**) under different temperatures in the presence of 60 ppm TNT and 100 μM OP, respectively. All error bars represent the s.d. from 3 sensors.

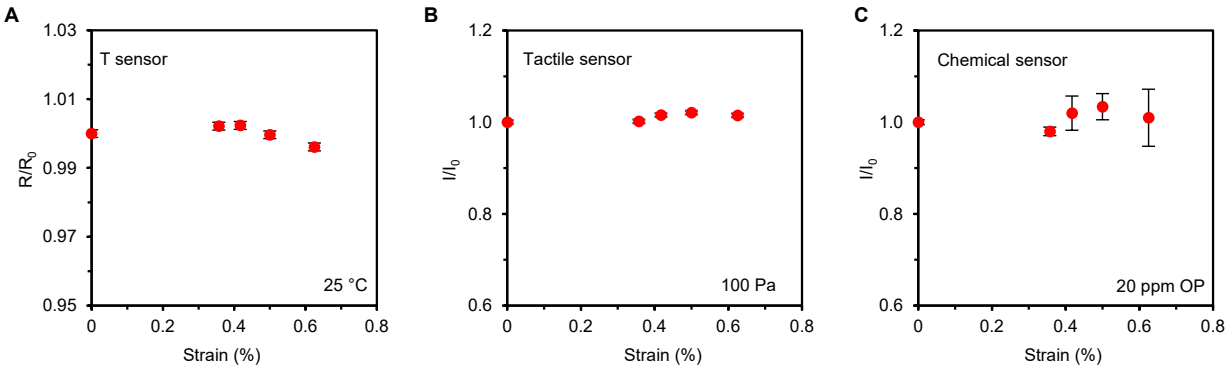

Fig. S22. Performance of the printed sensor arrays under mechanical deformation. (**A**–**C**) The response of the inkjet-printed temperature sensors (**A**), tactile sensors (**B**), and OP sensors (**C**) under varied strain (0 to 0.625%). R and R_0 represent the resistive response of the sensors after and before bending, respectively. I and I_0 represent the current response of the sensors after and before bending, respectively. All error bars represent the s.d. from 3 sensors.

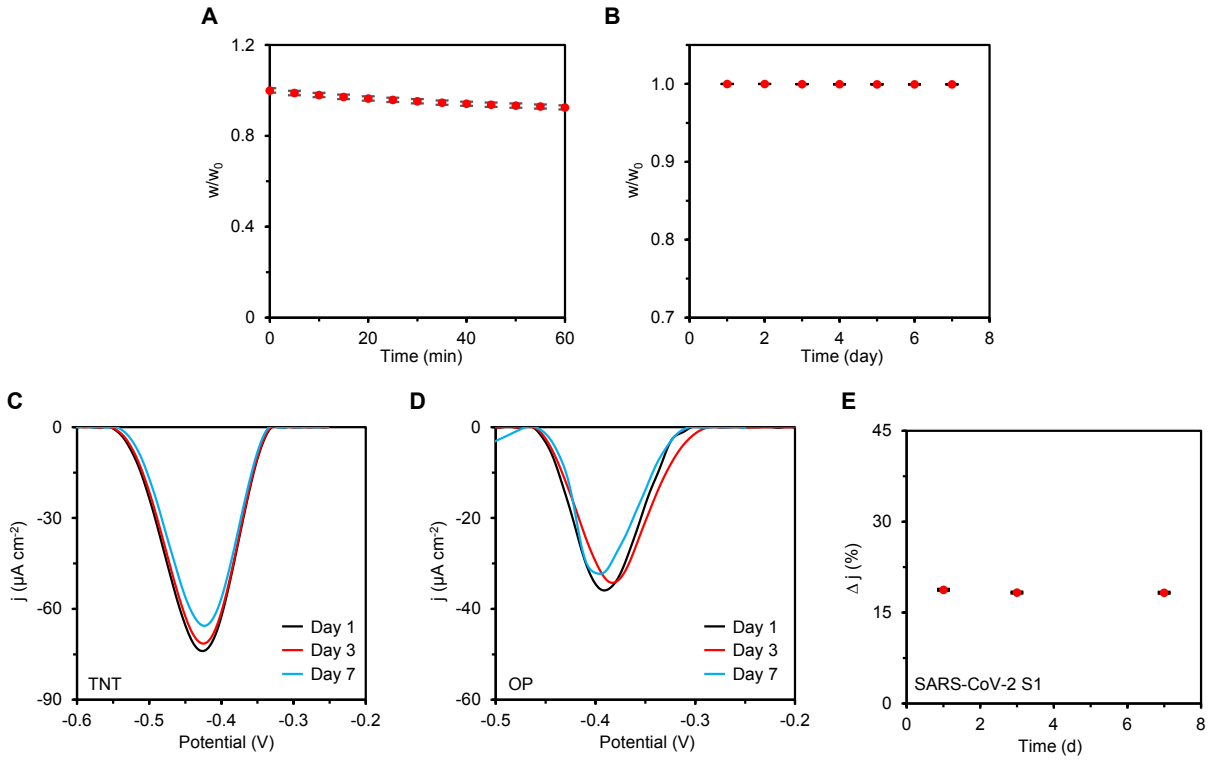

Fig. S23. **Stability of the hydrogel.** (**A** and **B**) The weight of the hydrogel under operation condition (**A**) and 4°C storage condition (**B**). W and W_0 represent the measured weight during test and the weight before the storage, respectively. (**C** and **D**) nDPV voltammograms of the Pt-graphene sensors for detecting 60 ppm TNT (**C**) and MOF-808/Au sensors for detecting 25 ppm OP (**D**) with fresh, 2-day, and 6-day aged hydrogels. Error bars represent the s.d. from 3 units. (**E**) Percentage DPV peak current changes of the CNT-based SARS-CoV-2 S1 sensor after target incubation.

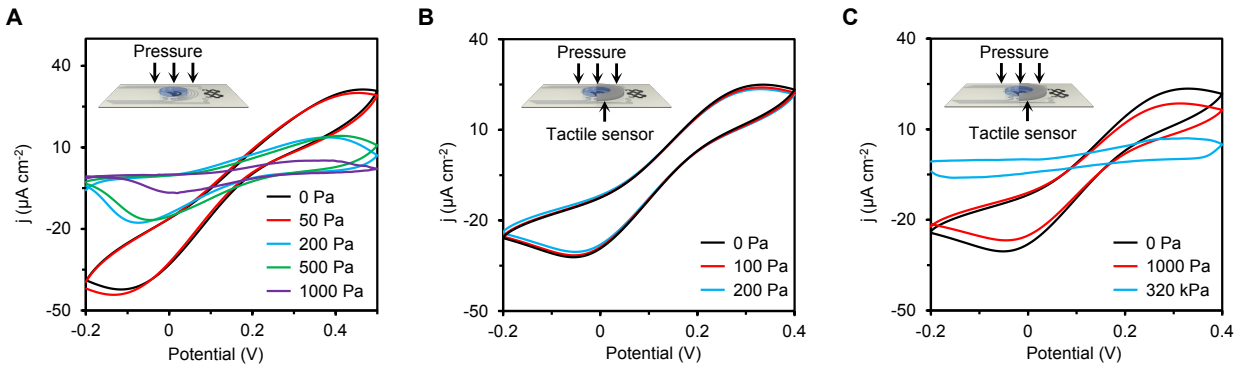

Fig. S24. Influence of the contact pressure on the electrochemical sensor performance. (**A**) The CVs obtained under varying contact pressure on a hydrogel-loaded IPCE. (**B** and **C**) The CVs obtained under varying contact pressure on a PDMS microwell (tactile sensor) protected hydrogel-loaded IPCE. 2 mM $K_3Fe(CN)_6$ was used as the model target. Scan rates, 50 mV s^{-1}.

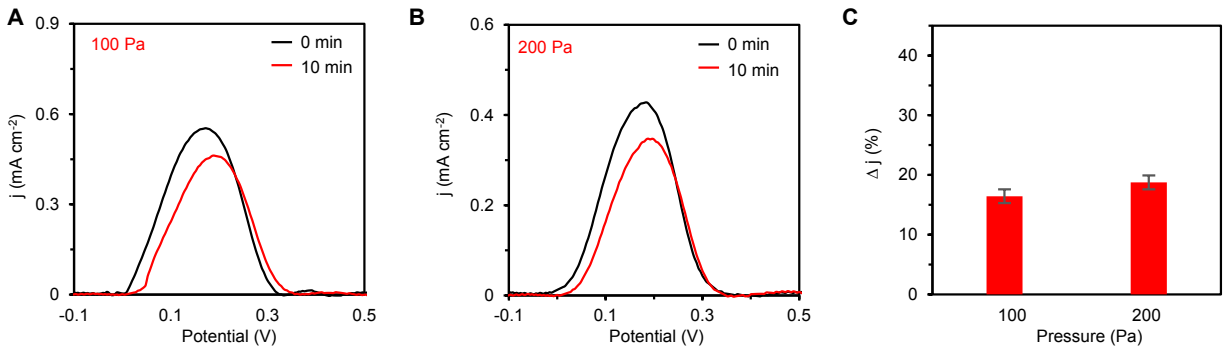

Fig. S25. **Interference of the contact pressure on SARS-CoV-2 S1 sensor performance. (A–C)** DPV voltammograms (**A** and **B**) of the SARS-CoV-2 S1 sensors and percentage DPV peak current changes (**C**) before and after target incubation under varying applied normal pressure. Error bars represent the s.d. from 3 sensors.

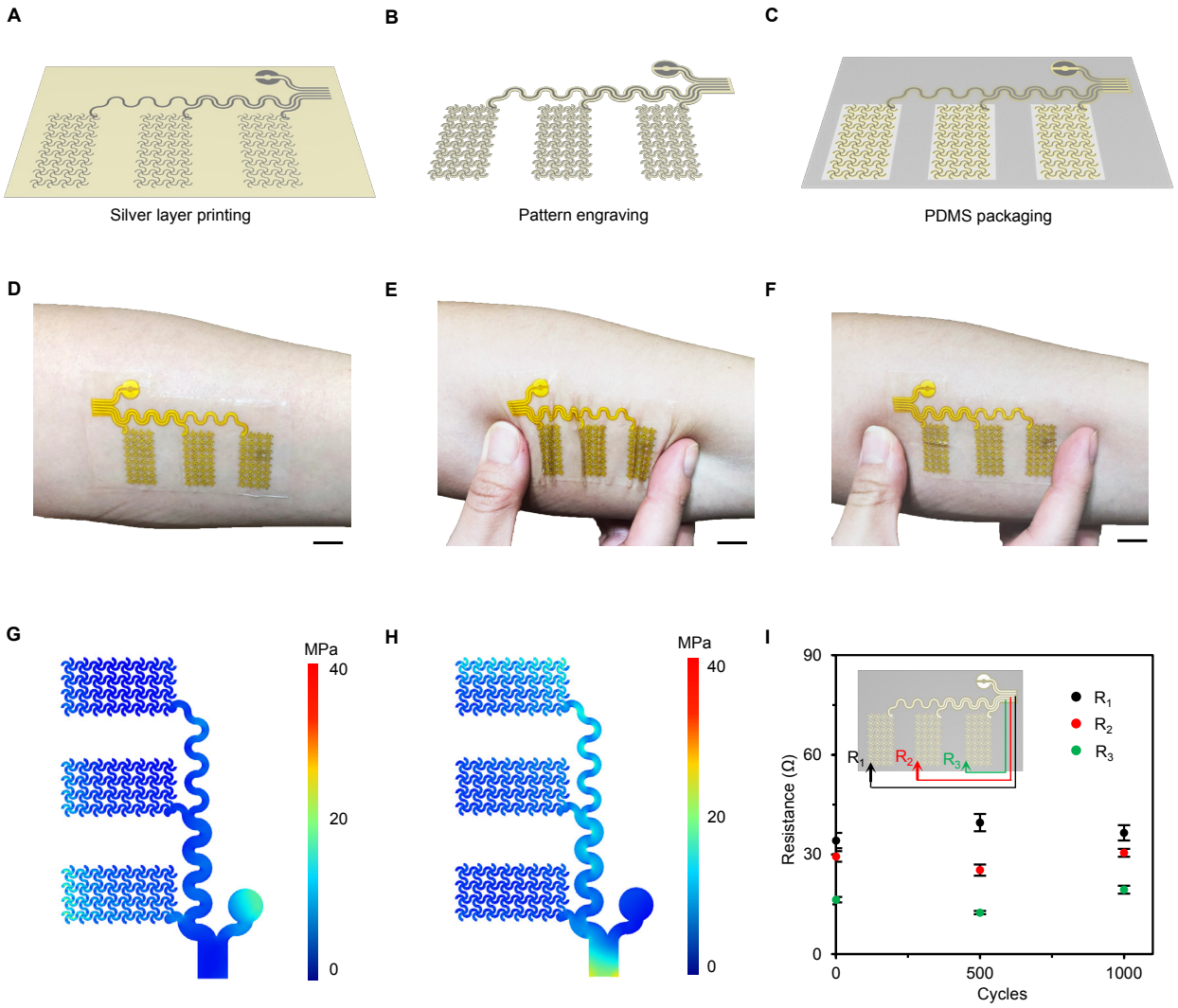

Fig. S26. Fabrication and characterization of the soft and stretchable e-skin-H. (**A–C**) Schematic fabrication process of the inkjet-printed, PDMS encapsulated e-skin-H. (**D–F**) Photographs of an e-skin-H on a subject's arm. Scale bars, 5 mm. (**G** and **H**) Numerical simulation showing the pressure distributions of e-skin-H under 1% strain along the horizontal and vertical axis. (**I**) The resistance between the sEMG electrodes and their connection pins after bending (with a radius of bending curvature of 1.5 cm). All error bars represent the s.d. from 3 measurements.

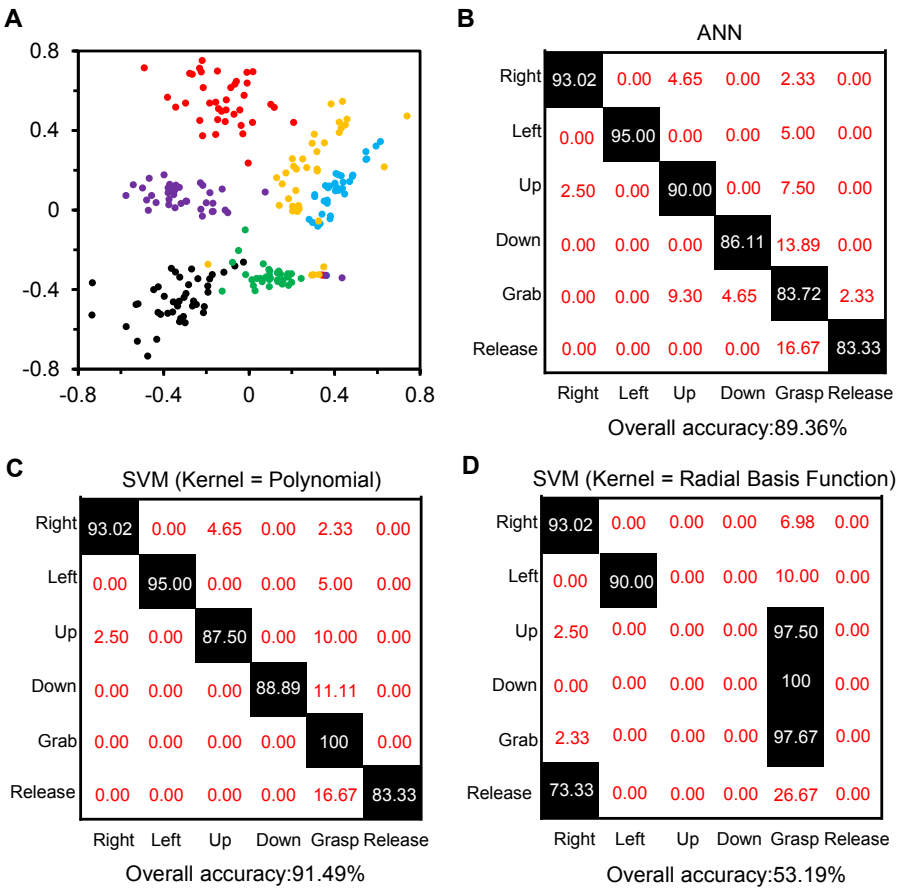

Fig. S27. Gesture classification confusion matrix obtained with different machine learning algorithms. (**A**) A 2-dimensional representation of the 4-dimensional feature set extracted from the sEMG recording. The multidimensional scaling from 4 dimensions to 2 dimensions was performed using the scikit-learn MDS API (version 0.24.2). (**B–D**) The gesture accuracy breakdown for hand movement using the artificial neural network (ANN) (**B**), the support vector machine (SVM) (polynomial kernel) (**C**), and the SVM (radial kernel) (**D**). Each row represents a hand movement that was performed, while each column represents what gesture the model labeled the movement. The values in each cell represent the percentage of time the movement (in the row) was labeled as the respective columns gesture.

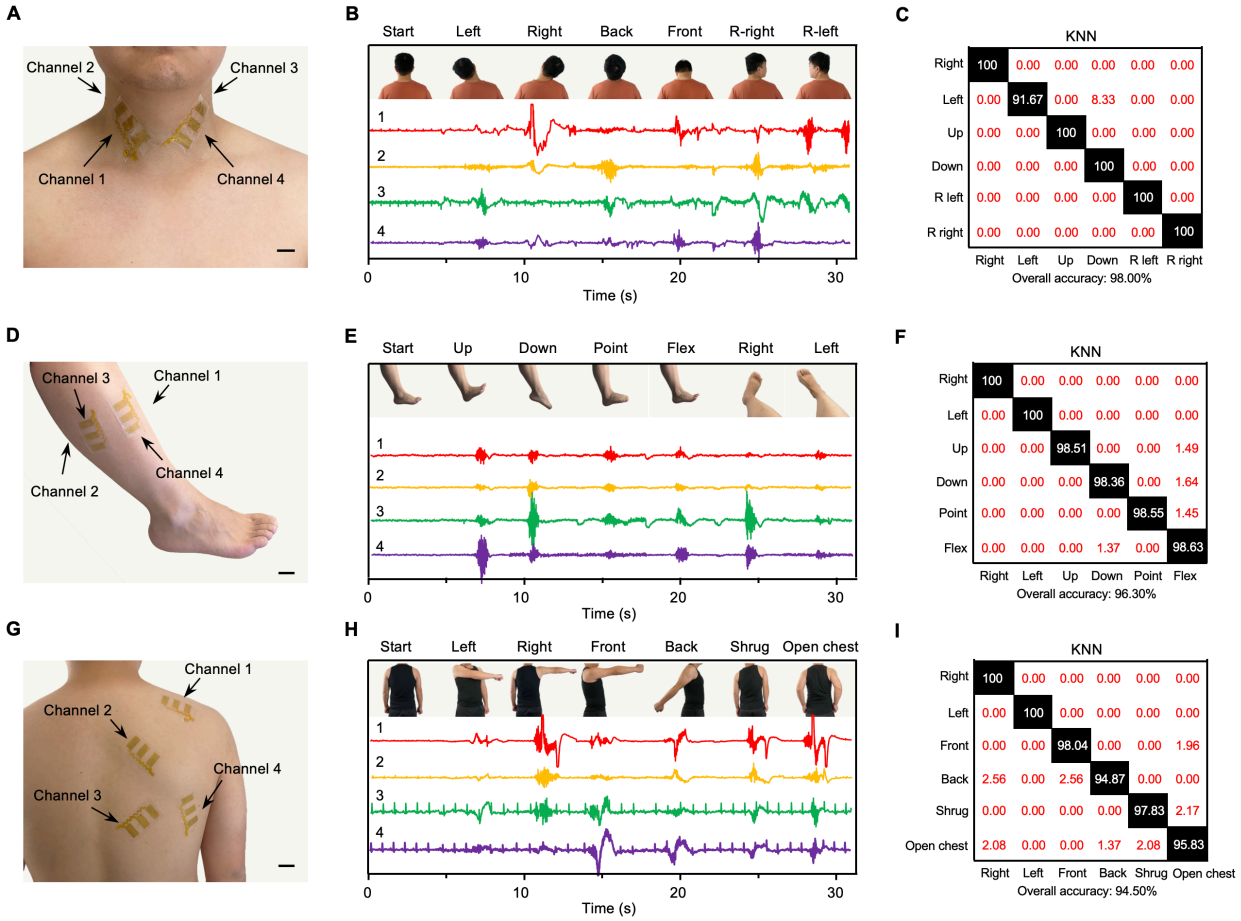

Fig. S28. Evaluation of the e-skin-H on different body parts for AI-assisted human-machine interaction. (**A**) Photograph of the e-skin-H on the neck. (**B** and **C**) sEMG data (**B**) and the corresponding classification confusion matrix using a KNN model (**C**) from the e-skin-H on the neck. (**D**) Photograph of the e-skin-H on the lower limb. (**E** and **F**) sEMG data (**E**) and the corresponding classification confusion matrix using a KNN model (**F**) from the e-skin-H on the lower limb. (**G**) Photograph of the e-skin-H on the upper back. (**H** and **I**) sEMG data (**H**) and the corresponding classification confusion matrix using a KNN model (**I**) from the e-skin-H on the upper back. Scale bars, 2 cm.

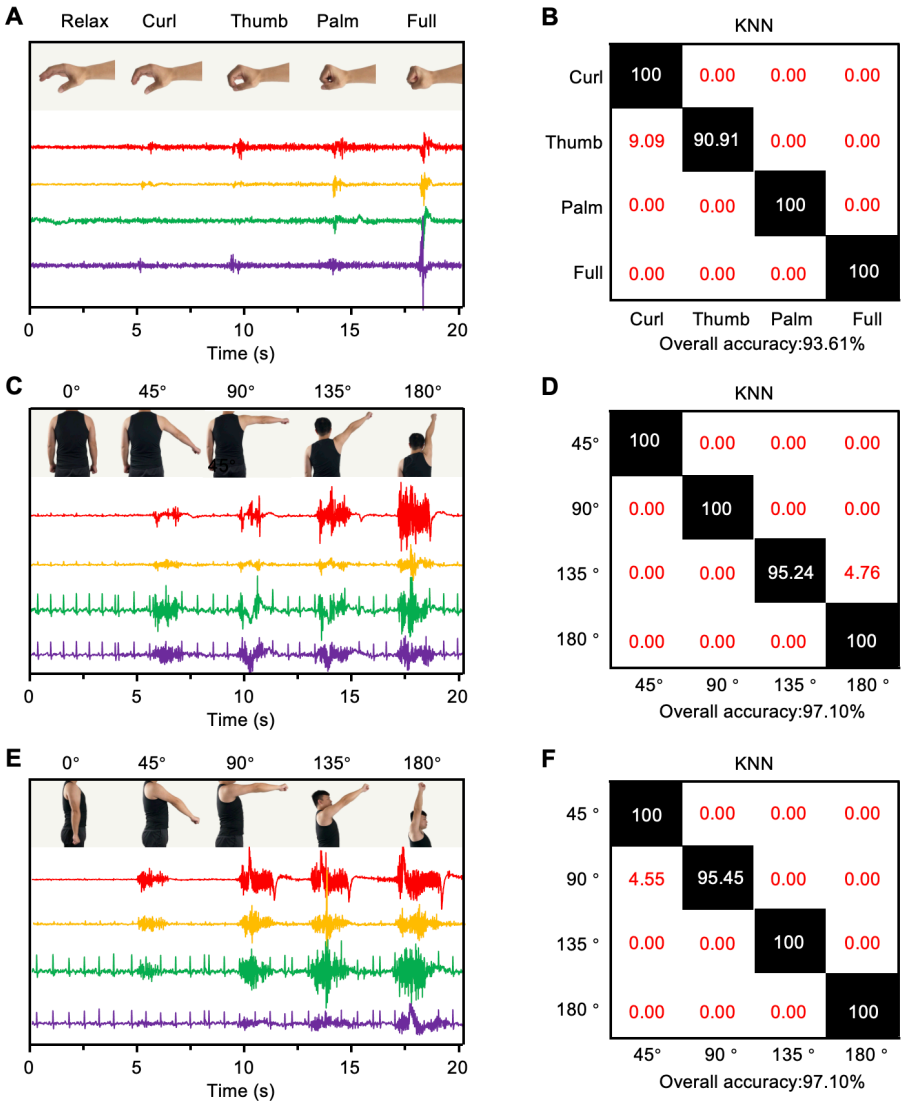

Fig. S29. **Evaluation of the e-skin-H from gestures with different degrees.** (**A** and **B**) sEMG data collected by the e-skin-H on the arm from 4 grasp degrees (**A**) and the corresponding classification confusion matrix using a KNN model (**B**). (**C** and **D**) sEMG data collected by the e-skin-H on the upper back from 4 right gesture degrees (**C**) and the corresponding classification confusion matrix using a KNN model (**D**). (**E** and **F**) sEMG data collected by the e-skin-H on the upper back from 4 front gesture degrees (**E**) and the corresponding classification confusion matrix using a KNN model (**F**).

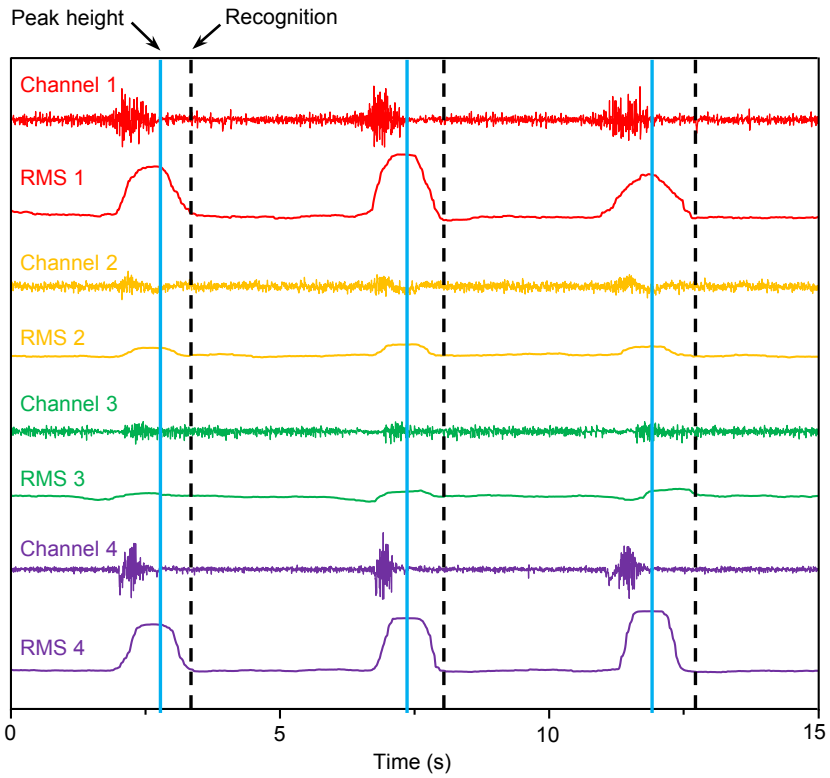

Fig. S30. sEMG and root mean square (RMS) data process for robotic hand control.

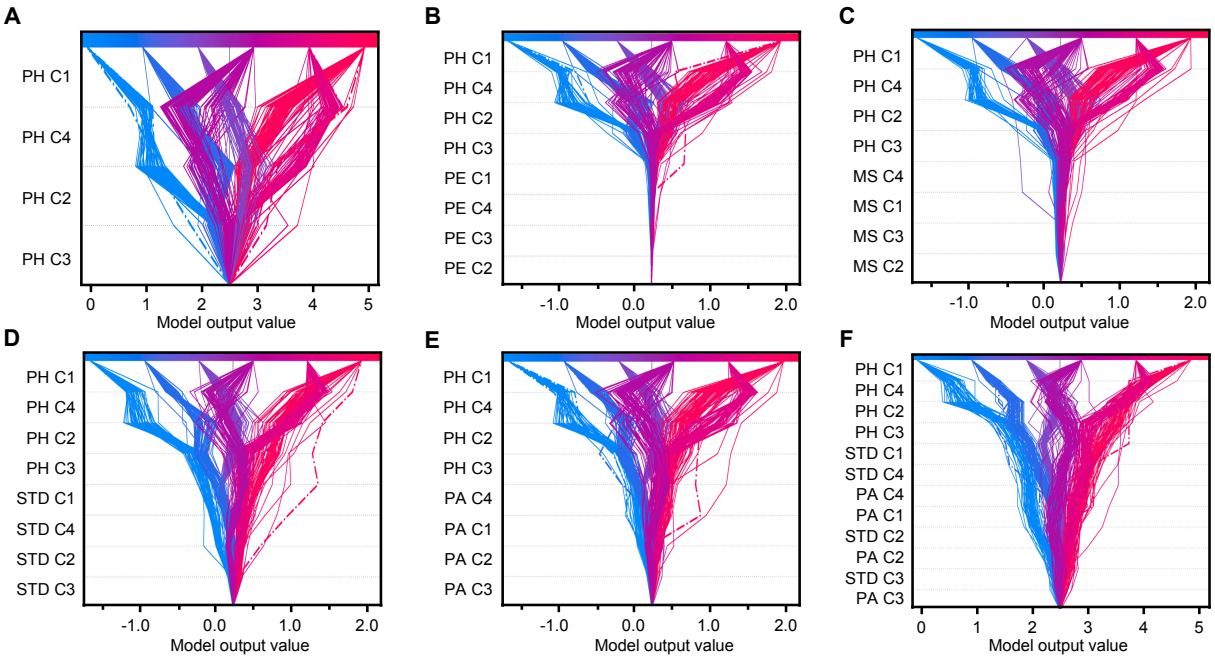

Fig. S31. SHAP decision plots based on the arm sEMG dataset with respect to a KNN classification model. (A–F) SHAP decision plots displaying the SHAP contribution of feature(s) in a KNN classification model: PH only (**A**), PH+PE (**B**), PH+MS (**C**), PH+STD (**D**), PH+PA (**E**), and PH+STD+PA (**F**). Each decision line tracks the respective features' contributions to every individual classification, represented as serialized integer that maps to a hand movement. Dotted lines represent misclassified points.

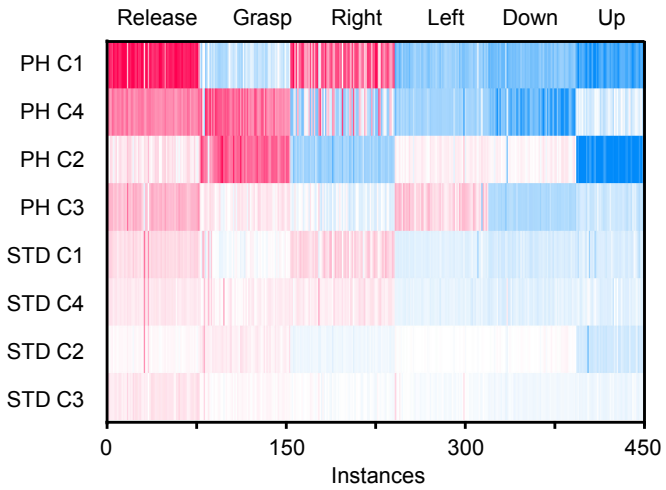

Fig. S32. A SHAP heatmap that clusters each point's SHAP value by its respective gesture classification. The value (color) of each feature represents its SHAP value (prediction contribution) for a given gesture. The sign of the SHAP value represents its movement with respect to an arbitrary base value (average of all serialized classifications). Because of the arbitrary base value, each column in the heatmap should be evaluated within its respective gesture.

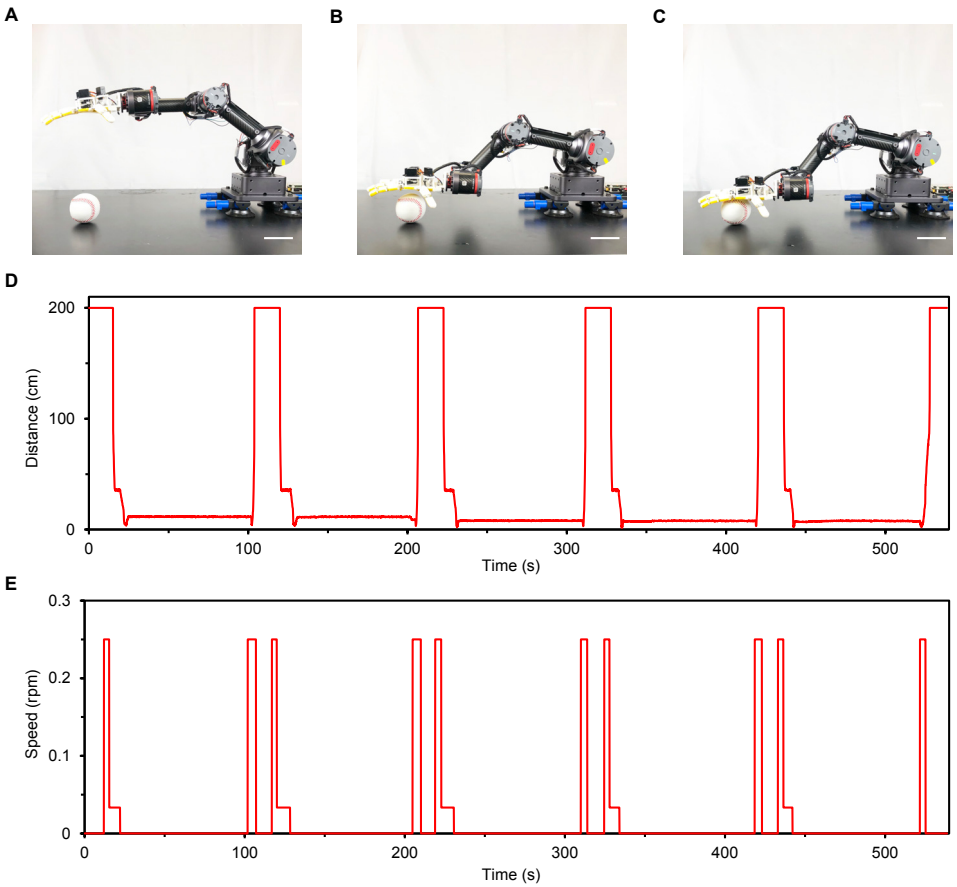

Fig. S33. Evaluation of the laser proximity sensor in robotic operation. (**A–C**) Photographs of a robotic hand approaching and touching a spherical object. Scale bars, 7 cm. (**D** and **E**) The response of the laser proximity sensor (**D**) and the rotating speed of the robotic arm (**E**) during multiple operation cycles of object approaching and touching.

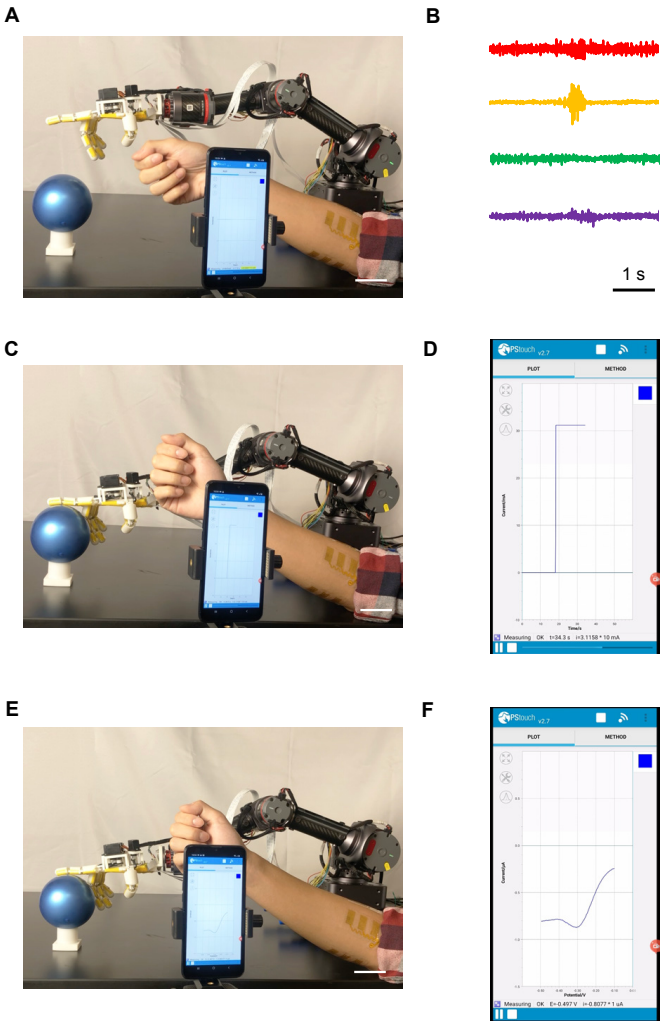

Fig. S34. Human-interactive robotic control for object touching and on-site TNT detection. (**A** and **B**) Image (**A**) and sEMG data (**B**) for robotic hand control to approach the object. (**C** and **D**) Image of the robotic finger contact (**C**) and the corresponding tactile sensor response (**D**). (**E** and **F**) Image of the finger-tip on-site TNT detection (**E**) and the collected nDPV voltammogram using a mobile interface (**F**). Scale bars, 5 cm.

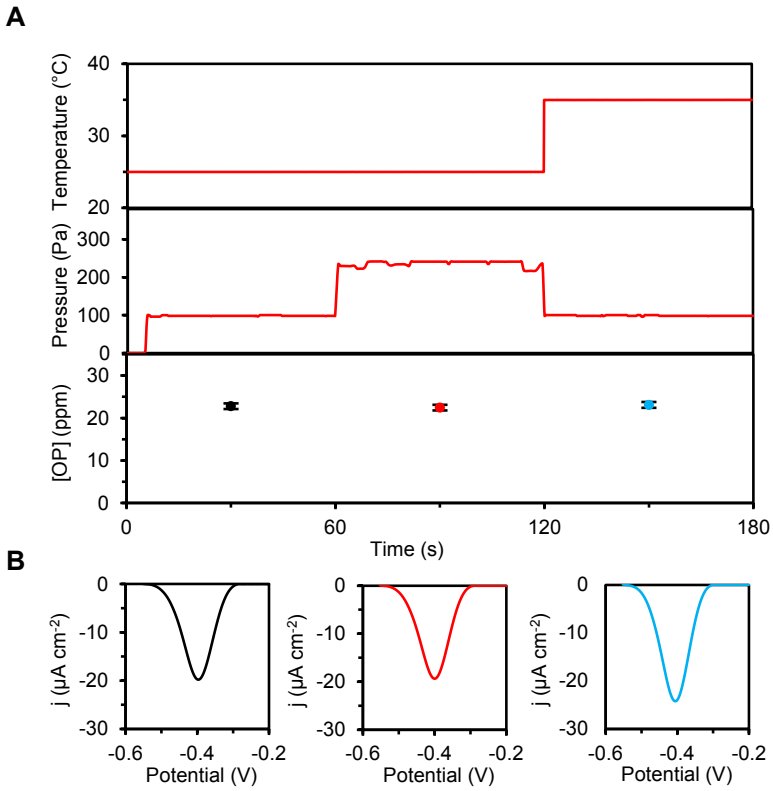

Fig. S35. **Multiplexed simultaneous physicochemical sensor analysis using the printed sensor array. (A)** Dynamic responses of temperature, tactile, and OP sensors for single point OP analysis. OP, 25 ppm. Contact pressure and temperature were altered during the sensing to study the signal interferences; temperature induced OP sensor response change was automatically calibrated. Error bars represent the s.d. from 3 sensors. (**B**) The nDPV voltammograms of the inkjet-printed MOF-808/Au sensor collected during the test.

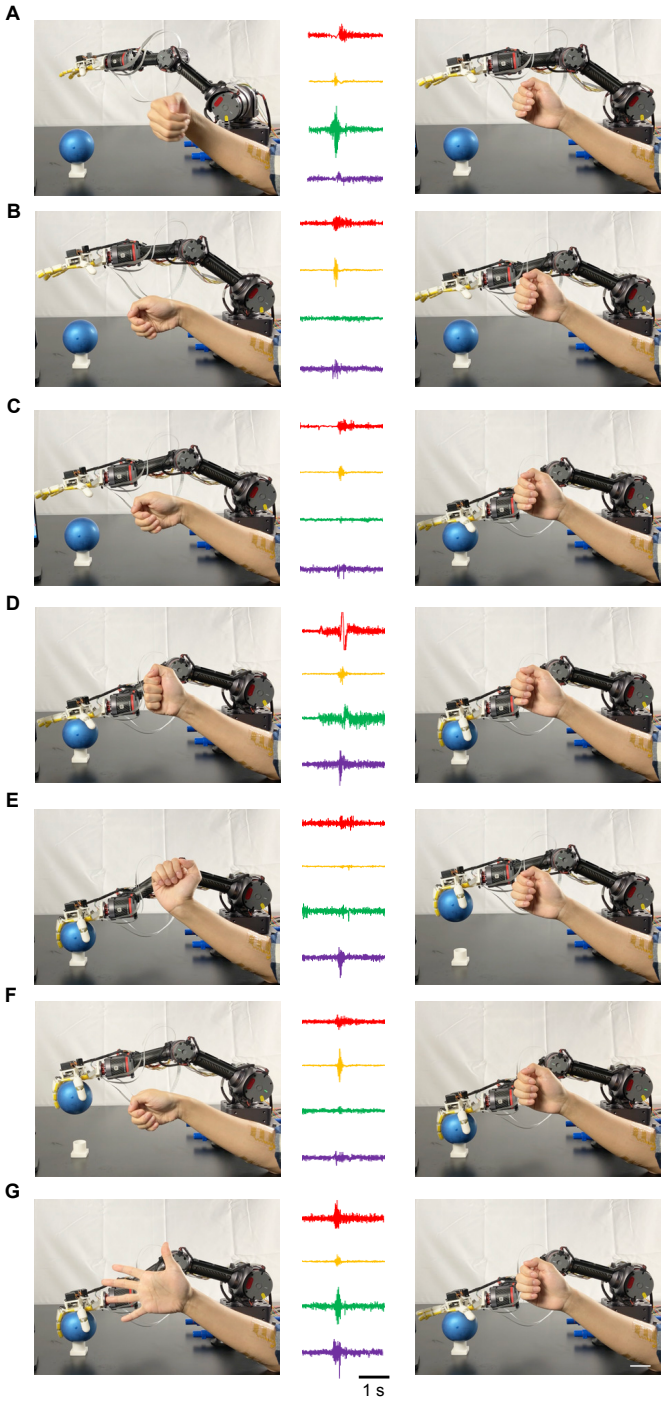

Fig. S36. Human-machine interactive robotic operation for object grasping. (A–G) the robotic hand operation for object grasping based on sEMG data collected from 7 sequential gesture controlled steps. Left column, hand gesture; middle column, sEMG data collected from the gesture; right column, machine learning assisted robotic hand operation. Scale bar, 5 cm.

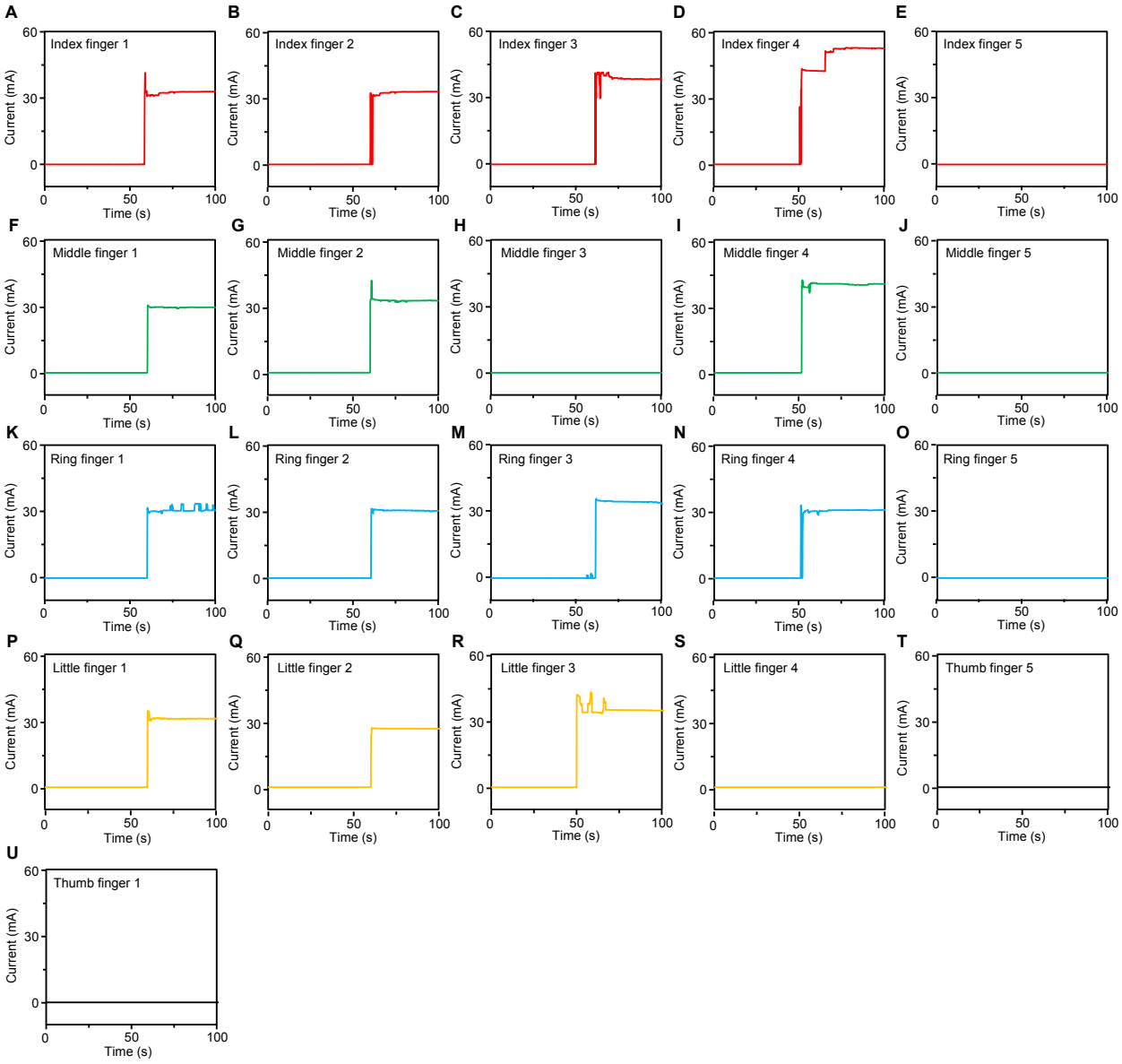

Fig. S37. **The tactile responses of the e-skin-R on a cylindrical object.** (A-E) Response of the tactile sensors on the index finger (A-E), the middle finger (F-J), the ring finger (K-O), the little finger (P-S), and the thumb finger (T and U).

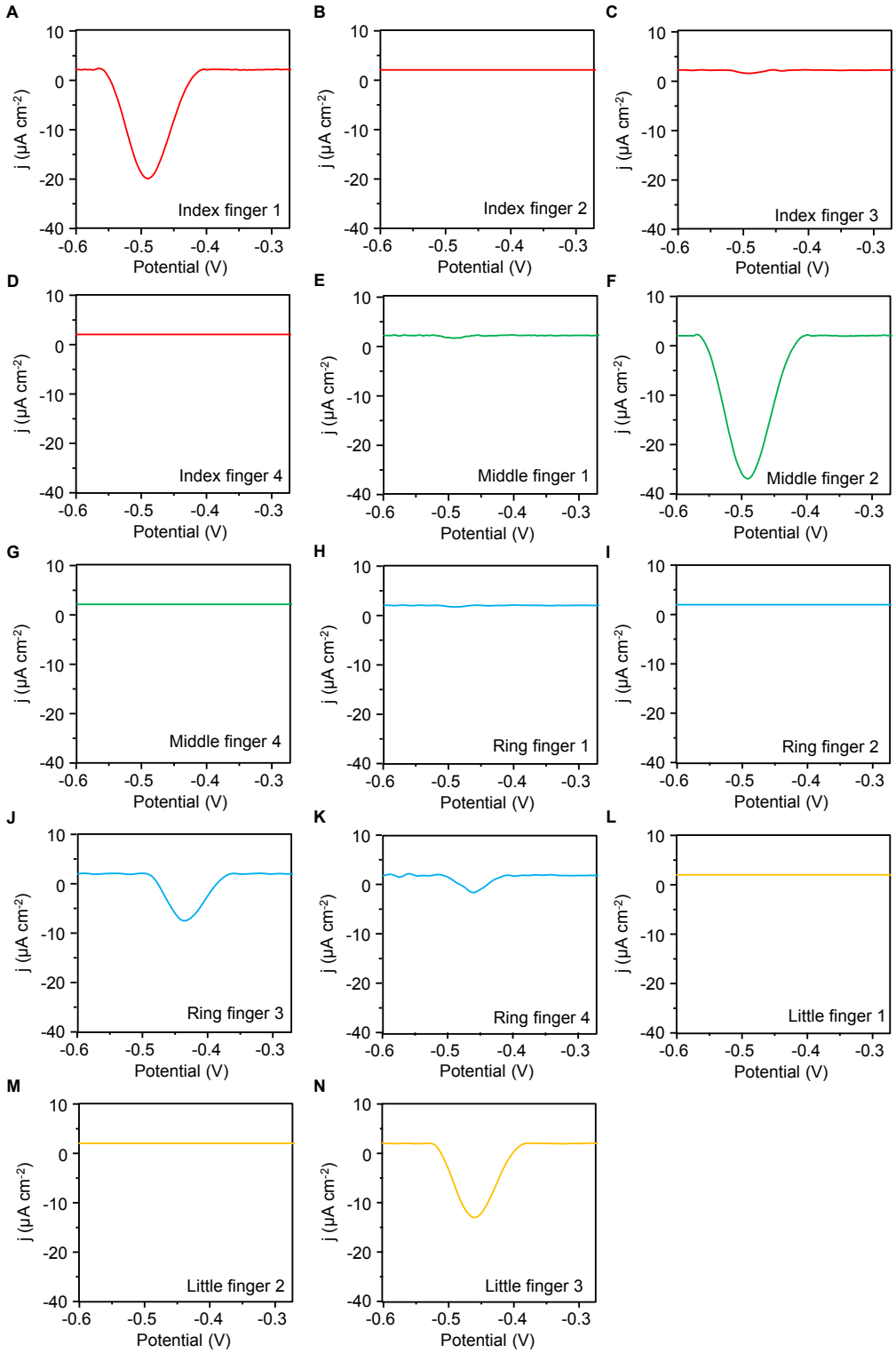

Fig. S38. **The OP sensing responses of the e-skin-R on a cylindrical object. (A–N)** nDPV responses of the MOF-808/Au sensors on the index finger (A-D), the middle finger (E-G), the ring finger (H-K), and the little finger (L-N).

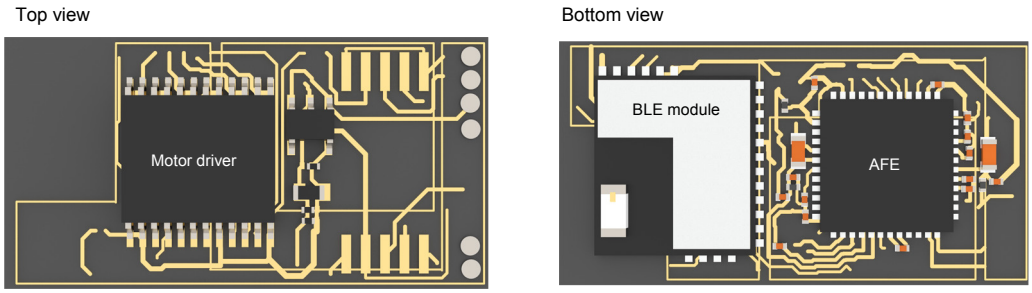

The list of components

Description	Value and series number	Number
BLE module	CYBLE-222014-01	1
Electrochemical front end	AD5941BCPZ	1
Motor driver	TB6612FNG	1
Voltage regulator	ADP162AUJZ-3.0-R7	1
Ferrite bead	BKP0603HS121-T	1
0201 Capacitor	220 pF	1
0201 Capacitor	0.1 μF	7
0201 Capacitor	0.47 μF	4
0201 Capacitor	1 μF	3
0201 Capacitor	4.7 μF	1
0402 Capacitor	10 μF	4
0201 Resistor	0 Ω	2
0201 Resistor	2.2 Ω	2
0201 Resistor	600 kΩ	1

Fig. S39. Schematic illustration and component list of the electronic system of the M-Boat.

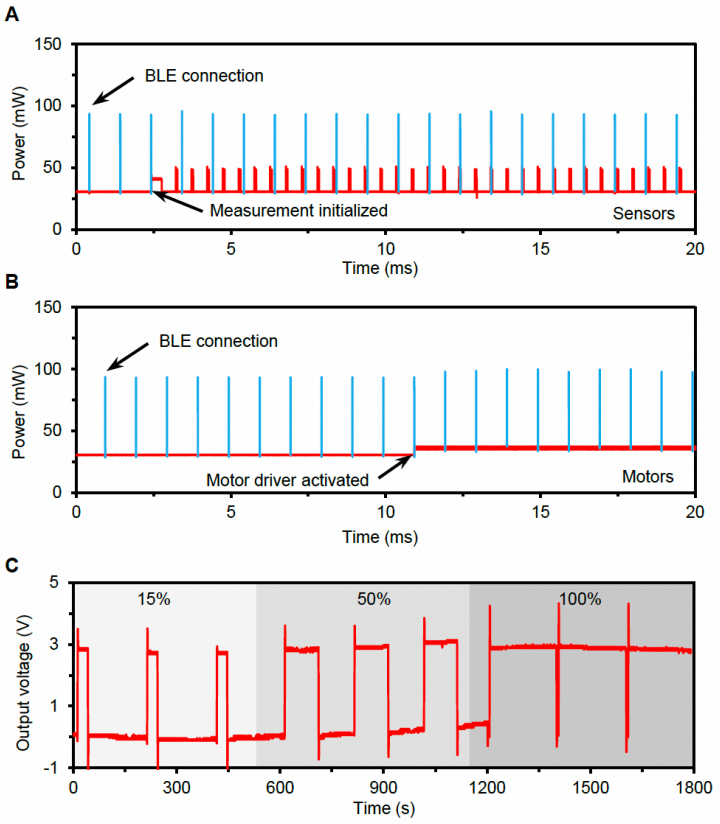

Fig. S40. **Characterization of the operation of the M-Boat.** (**A**) Power consumption of the M-Boat during the sensing mode. (**B**) Power consumption of the M-Boat during the propulsion mode. (**C**) Voltage output of the motor driver at 15%, 50 %, and 100% load (motor control was achieved by pulse width modulation).

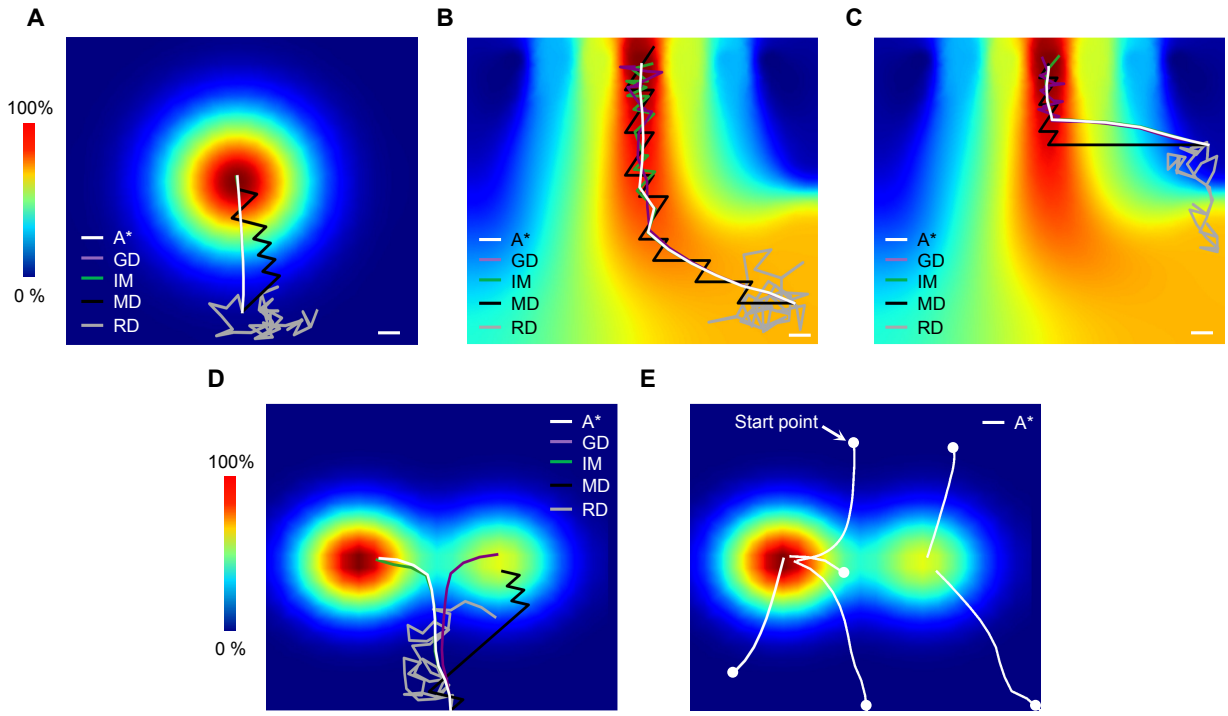

Fig. S41. **Simulation comparison of the searching algorithms for M-Boat autonomous source locating.** (**A–C**) Simulation comparison of the searching algorithms for M-Boat autonomous source locating when one source is present. (**D** and **E**) Simulated paths the M-Boat would follow using different algorithms at the same starting location (**D**) and using A* algorithm at different starting locations (**E**) when two sources (unequal in magnitude) are present.

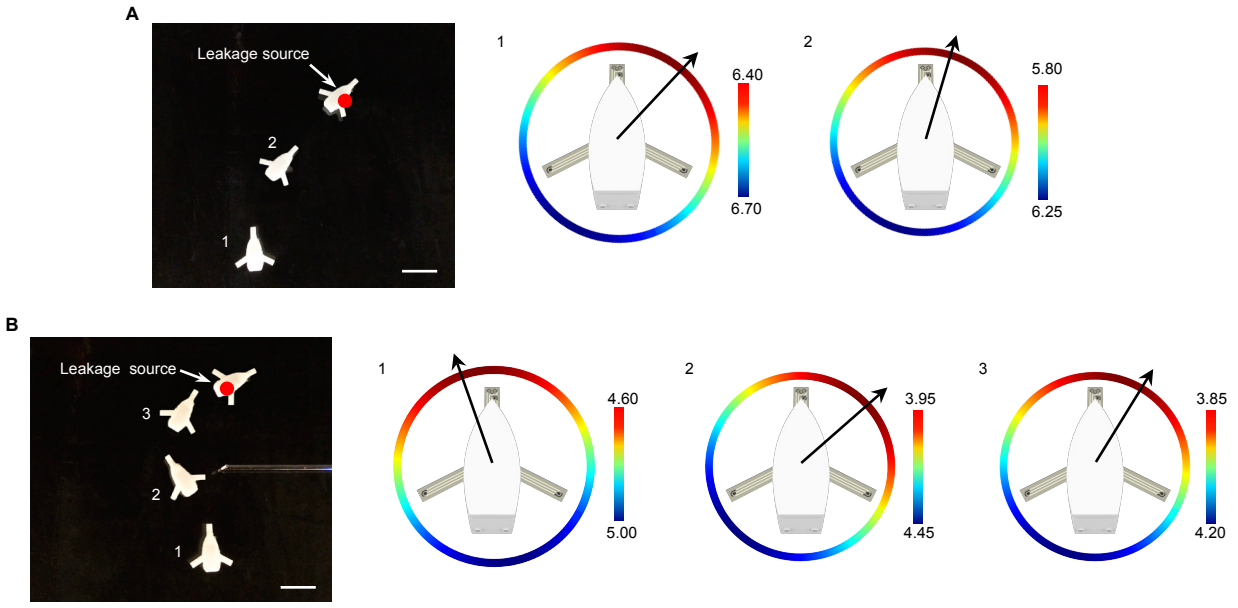

Fig. S42. Evaluation of the M-Boat for autonomous source tracking. Time lapse images of the M-Boat-based source tracking and the data collected at each decision-making point (**A** and **B** represent data collected from two independent trials). Scale bars, 5 cm.

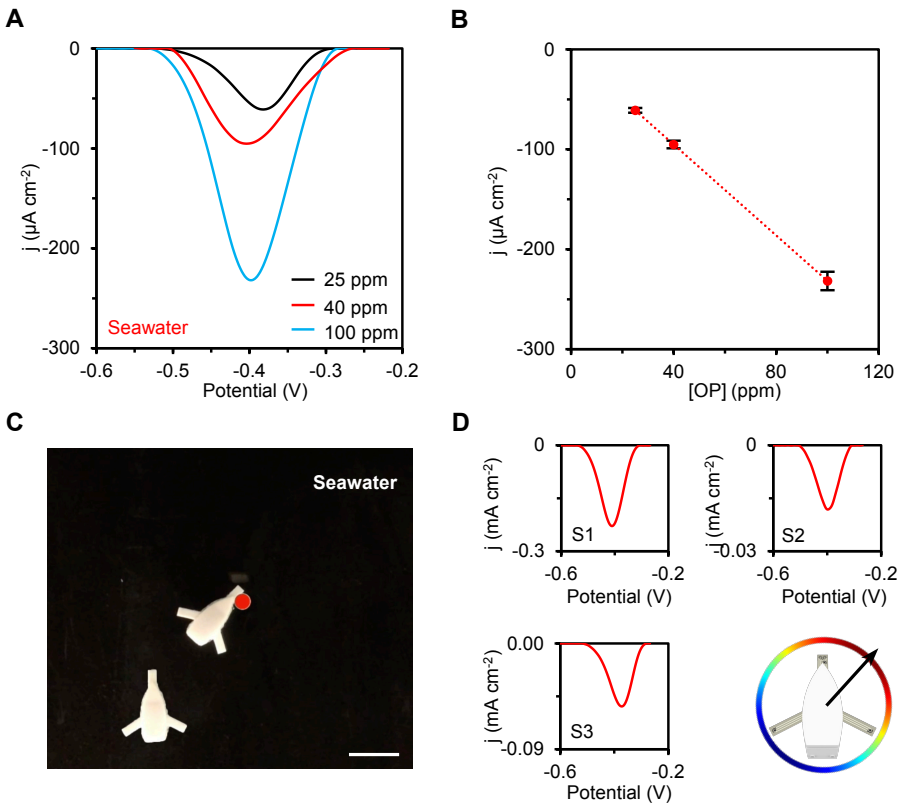

Fig. S43. **Evaluation of the M-Boat in seawater.** (**A** and **B**) nDPV voltammograms of the inkjet-printed OP sensor in seawater with spiked OP (25–100 ppm) (**A**) and the corresponding calibration curves (**B**). Error bars represent the s.d. from 3 sensors. (**C**) Time lapse images showing the operation of the M-Boat in seawater for autonomous OP source tracking. Scale bar, 5 cm. (**D**) nDPV voltammograms collected by the M-Boat's OP sensors in seawater and the resulted algorithm-driven decision-making for autonomous source tracking.

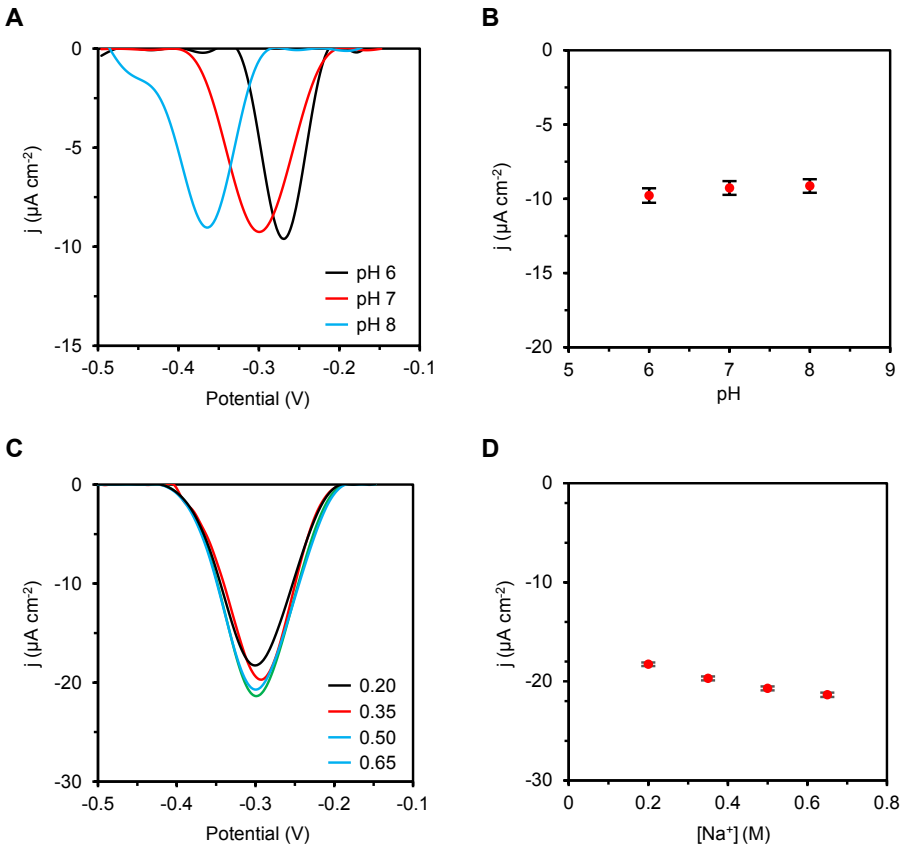

Fig. S44. **Influence of ionic strength and pH on sensor performance.** (**A** and **B**) The nDPV voltammograms (**A**) and the corresponding calibration plot (**B**) of the OP sensors in solutions with 15 ppm OP and different pHs (6 to 8). (**C** and **D**) nDPV voltammograms (**C**) and the corresponding calibration plot (**D**) of the OP sensors in 25 ppm OP and varing sodium concentrations (from 0.20 M to 0.65 M). Error bars represent the s.d. from 3 sensors.

Table S1. Ink composition and characterizations.

	Surface tension (mN m^{-1})	Viscosity (mPa*s)	Density (g ml^{-1})	Inverse Ohnesorge number	Thermal annealing (°C)
Ag (25 wt%)	31.0	8	1.3	3.6	240
Au (10 wt%)	30.0	10	1.1	2.6	180
C (5 wt%)	32.5	10	1.1	2.7	240
AgNWs (2 mg ml^{-1})	21.5	2	0.8	9.6	150
PAA (3 wt%)	42.8	11	1.1	2.8	250
GO (2 mg ml^{-1})	53.9	6	1.1	5.8	180
MOF-808 (2 mg ml^{-1})	56.6	3	1.0	11.7	180
CNT (2 mg ml^{-1})	55.5	7	1.0	4.9	120

Data measured at 25°C; inverse Ohnesorge number: $Z = \frac{\sqrt{\sigma \rho d}}{\eta}$; d (diameter of the nozzle) = 21 μm; σ, surface tension; ρ, density; η, viscosity.

Table S2. Accuracy breakdown per feature with and without one channel removed. The values reported represent the mean accuracy ± the standard deviation (%) of the KNN trained using the arm EMG dataset across 5000 trials. 3 features: PH, STD, and PA. 5 features: PH, STD, MS, PA, PE.

	5 features	3 fearures	PH	STD	MS	PA	PE
All channels	97.29±1.11	97.28±1.14	97.20±1.12	97.02±1.17	93.05±1.69	92.49±1.76	88.71±2.05
No channel1	96.31±1.25	96.45±1.25	96.65±1.15	96.04±1.28	90.44±1.85	90.55±1.86	87.47±2.16
No channel2	89.99±1.83	89.18±1.96	88.65±1.92	88.19±1.92	84.32±2.04	81.21±2.29	84.10±2.30
No channel3	92.63±1.83	91.96±1.86	90.23±1.91	90.64±1.81	84.31±2.25	79.39±2.77	76.94±2.71
No channel4	94.84±1.50	94.75±1.52	94.13±1.51	94.36±1.47	85.95±2.26	86.86±2.27	82.18±2.66

Table S3. Accuracy breakdown based on five features with one and two channels. The values reported represent the mean accuracy ± the standard deviation (%) of the KNN trained using the arm EMG dataset across 5000 trials.

	Channel 1	Channel 2	Channel 3	Channel 4
Channel 1	52.53±3.12	80.05±2.55	79.44±2.32	76.74±2.57
Channel 2	80.05±2.55	56.32±3.09	85.81±2.45	86.05±2.25
Channel 3	79.44±2.32	85.81±2.45	68.42±3.41	87.37±1.88
Channel 4	76.74±2.57	86.05±2.25	87.37±1.88	65.35±2.72

Supporting Movies

Movie S1. Inkjet-printed soft e-skin for human-machine interaction and multimodal sensing

Movie S2. Machine learning-assisted human-interactive robotic control

Movie S3. M-Bot: Human-machine interactive robotic fingertip point of sensing

Movie S4. M-Bot: Human-machine interactive robotic object manipulation and on-site hazard analysis

Movie S5. M-Boat: Wireless motion control

Movie S6. M-Boat: Autonomous source tracking